Mitophagy inhibits amyloid-β and tau pathology and reverses cognitive deficits in models of Alzheimer's disease

Evandro F. Fang[1,2,12,*], Yujun Hou[1,12], Konstantinos Palikaras[3,12], Bryan A. Adriaanse[4], Jesse S. Kerr[1], Beimeng Yang[1], Sofie Lautrup[1], Md Mahdi Hasan-Olive[2], Domenica Caponio[2], Xiuli Dan[1], Paula Rocktäschel[4], Deborah L. Croteau[1], Mansour Akbari[5], Nigel H. Greig[6], Tormod Fladby[7,8], Hilde Nilsen[2], M. Zameel Cader[4], Mark P. Mattson[9,10], Nektarios Tavernarakis[3,11], Vilhelm A. Bohr[1,5,*]

[1]Laboratory of Molecular Gerontology, National Institute on Aging, National Institutes of Health, Baltimore, MD 21224, USA
[2]Department of Clinical Molecular Biology, University of Oslo and Akershus University Hospital, 1478 Lørenskog, Norway
[3]Institute of Molecular Biology and Biotechnology, Foundation for Research and Technology-Hellas, Greece
[4]Weatherall Institute of Molecular Medicine, University of Oxford, Oxford OX3 9DS, UK
[5]Danish Center for Healthy Aging, University of Copenhagen, Blegdamsvej 3B, 2200 Copenhagen, Denmark
[6]Translational Gerontology Branch, National Institute on Aging, National Institutes of Health, Baltimore, MD 21224, USA
[7]Division of Medicine and Laboratory Sciences, Institute of Clinical Medicine, Faculty of Medicine, University of Oslo, Oslo, Norway
[8]Department of Neurology, Akershus University Hospital, Lørenskog, Norway
[9]Laboratory of Neurosciences, National Institute on Aging, National Institutes of Health, Baltimore, MD 21224, USA
[10]Department of Neuroscience, Johns Hopkins University School of Medicine, Baltimore, Maryland 21205, USA
[11]Department of Basic Sciences, Faculty of Medicine, University of Crete, Heraklion, 70013, Crete, Greece

[12]These authors contributed equally to this work.

*Corresponding authors:
Evandro F. Fang (e.f.fang@medisin.uio.no)
Vilhelm A. Bohr (bohrv@grc.nia.nih.gov)

ORCID:
Evandro Fei Fang: 0000-0003-0355-7202
Yujun Hou: 0000-0003-1778-1176
Konstantinos Palikaras: 0000-0001-6992-5560
Vilhelm Bohr: 0000-0003-4823-6429

Abstract

Accumulation of damaged mitochondria is a hallmark of aging and age-related neurodegeneration, including in Alzheimer's disease (AD). The molecular mechanisms of impaired mitochondrial homeostasis in AD are being investigated. Here we provide evidence that mitophagy is impaired in AD patient hippocampus, in iPSC-derived human AD neurons and in animal AD models. In both Aβ and Tau *C. elegans* models of AD, mitophagy stimulation (through NAD^+ supplementation, urolithin A, and actinonin), reverses memory impairment through PINK1, PDR-1 or DCT-1 dependent pathways. Mitophagy diminishes insoluble $Aβ_{1-42}$ and $Aβ_{1-40}$ and prevents cognitive impairment in an APP/PS1 mouse model through microglial phagocytosis of extracellular Aβ plaques and suppression of neuroinflammation. Mitophagy enhancement abolishes AD-related Tau hyperphosphorylation in human neuronal cells and reverses memory impairment in transgenic Tau nematodes and mice. Our findings suggest that impaired removal of defective mitochondria is a pivotal event in AD pathogenesis and mitophagy representing a novel therapeutic intervention.

Introduction

Mitochondria produce the necessary ATP for survival and optimal function of neurons, and mitochondrial dysfunction is associated with aging and neurodegenerative diseases[1, 2]. In AD, neurons experience mitochondrial dysfunction and a bioenergetic deficit that may contribute to the disease-defining Aβ and hyper-phosphorylated Tau (p-Tau) pathologies; conversely, Aβ and Tau pathologies can promote mitochondrial defects[2, 3]. Impairment of mitochondrial function is a fundamental phenomenon in AD as it exists in human samples of both sporadic and familial types of the disease, as well as in brain tissues of transgenic AD mouse models[2, 4]. At the cellular level, non-glycosylated full-length amyloid precursor protein (APP) and C-terminal truncated APP anchor in the mitochondrial protein import channels (TOM40 and TIM23), blocking the entry of nuclear-encoded mitochondrial proteins[5]. Mitochondrial dysfunction-induced energy deficiency and $Aβ_{1-42}$ oligomers trigger intracellular Ca^{2+} imbalance and AMP-activated kinase (AMPK) activation, leading to synaptotoxicity and memory loss[2, 6]. Furthermore, while axonal transport of mitochondria is critical for neuronal function, $Aβ_{1-42}$ and p-Tau induce defects in axonal transport, resulting in synapse starvation, ATP depletion and ultimately neurodegeneration[7-9]. Thus, there is a sophisticated set of connections between mitochondrial impairment and these two AD pathologic factors, suggesting that targeting defective mitochondria may be an important approach for AD therapy.

Mitochondrial quality control is regulated by the processes of mitochondrial biogenesis and mitophagy. Mitophagy involves the targeting of damaged or superfluous mitochondria to the lysosomes wherein the mitochondrial constituents are degraded and recycled[10, 11]. In mammals, over 20 proteins have been reported as necessary for mitophagy, including PINK1, Parkin, ULK1, NIX/BNIP3L, and TBK1[2]. Commensurate with an age-dependent increase of the incidence of AD, there is also an age-dependent accumulation of dysfunctional mitochondria and impaired mitophagy[2]. Importantly, mitophagy plays a critical role in neuronal function and neuronal survival through the maintenance of a healthy mitochondrial pool and the inhibition of neuronal death[11, 12]. However, the role of mitophagy in AD progression is unclear. Utilizing postmortem human AD brain samples, AD induced pluripotent stem cell (iPSC)-derived neurons,

and transgenic animal models of AD, we show defective mitophagy in AD. Furthermore, the restoration of mitophagy ameliorates memory loss in both *C. elegans* and two mouse models of AD through the inhibition of Aβ plaques and p-Tau. Here we propose that defective mitophagy induces accumulation of dysfunctional mitochondria promoting AD pathology and memory loss, and suggest that it is a druggable target.

Results

Defective mitophagy in AD patient hippocampal samples and in AD iPSC-derived neurons

To uncover the cellular and molecular causes of mitochondrial impairment and the accumulation of damaged mitochondria in AD, we examined neuronal mitochondrial morphology in postmortem hippocampal tissues from age- and sex-matched AD patients and healthy individuals (patient information in Supplementary Table 1). Hippocampal neurons in AD samples displayed altered mitochondrial morphology characterized by reduced size and excessive mitochondrial damage compared to healthy controls (Fig. 1a, b). Dysfunctional mitochondria are less efficient at energy production, resulting in ATP depletion and stimulation of AMPK, an evolutionarily conserved master regulator of energy expenditure and mitochondrial homeostasis[13-15]. In wild type (WT) cells, activated AMPK coordinates mitochondrial fragmentation through stimulation of mitochondrial fission factor (MFF), and mitophagic clearance of defective organelles in response to bioenergetic stress[14, 15]. In human AD hippocampal tissue, we detected a large increase in the activity of AMPK and its downstream effector MFF (Fig. 1c, and quantification in Supplementary Fig. 1a). Interestingly, the basal levels of mitophagy in AD hippocampus were 30%-50% lower than normal as monitored by the co-localization of the mitochondrial protein TOMM20 with LAMP2 lysosomal protein and quantification of mitophagy-like events using electron microscopy (EM) (Fig. 1d, e, and Supplementary Fig. 1c). These findings show accumulation of damaged mitochondria in AD patient hippocampus possibly due to defective mitophagy.

Mitophagy impairment in AD may occur despite AMPK activation and abundance of smaller mitochondria, expected to be more readily removed by autophagic engulfment[11, 14, 15]. To address this apparent paradox, we systematically examined protein levels of major factors involved in mitochondrial metabolism and mitophagy[2]. Mitophagy proteins PINK1, Bcl2L13, and NIX/BNIP3L were decreased in some AD individuals, and mitophagy initiation proteins p-TBK1 (S^{172})[16] and p-ULK1 (S^{555})[15] were inactivated in all human AD samples (Fig. 1f and Supplementary Fig.1b). To investigate whether mitophagy is impaired in AD neurons, we established iPSC-derived neuronal cultures[17] using a familial AD (APP/V717L), a sporadic AD (APOE4/E4), and an age- and sex-matched healthy control (SBAD03-01) cell line (Fig. 1g-i). Using a well-established protocol[17, 18], we generated cortical neurons as evidenced by the expression of dendritic marker MAP2, neuron-specific tubulin maker Tuj1, and the cortical upper layer marker BRN2 (Fig. 1h-i, healthy control neurons). We further confirmed the maturation of neuronal identity in the APOE4- and the APP-derived neurons as evidenced by the expression of synaptophysin (a marker for presynaptic terminals, Supplementary Fig. 1d) and PSD-95 (a marker of postsynaptic density in glutamatergic neurons, Supplementary Fig. 1e). Furthermore, we found that AD iPSC-derived neurons recapitulate cellular features seen in human AD brain tissues, including increased DNA damage (higher γ-H2AX signal), compromised mitochondrial homeostasis (lower SIRT1, PGC1α, and SOD2), increased mitochondrial

fragmentation (higher p-DRP1 S^{616} and p-MFF S^{146}), and low ATP levels (Supplementary Fig.1e-h). Importantly, phosphorylation of mitophagic proteins TBK1 and ULK1 was reduced by more than 50% in AD as compared to control neurons (Fig. 1j and quantification in Supplementary Fig. 1g). Reduction of p-TBK1 (S^{172}) was conserved also in a PSEN1 line-derived cortical neurons (Supplementary Fig. 1d). Additionally, levels of other major mitophagy proteins, such as AMBRA1, Bcl2L13, FUNDC1, and MUL1[2] were decreased in AD iPSC-derived neuronal cells (Supplementary Fig.1f). Notably, basal levels of autophagy were diminished in AD neurons (lower levels of LC3-II and Beclin-1 in Fig. 1j and quantification in Supplementary Fig. 1g), which is in accord with previous reports[19]. Furthermore, we quantified autophagic flux using a monomeric red fluorescent protein (mRFP)-GFP tandem fluorescent-tagged LC3 plasmid (ptfLC3)[11, 20], with the data showing reduced numbers of both autophagosomes and autolysosomes in the APP neurons compared to controls (Supplementary Fig.1i). These results suggest a normal autophagic flux, but the overall induction of the autophagy pathway was reduced. Thus, we detect impairment of mitophagy both in AD patient hippocampal samples and in AD iPSC-derived neurons.

Restoration of neuronal mitophagy ameliorates cognitive decline in *C. elegans* models of AD

Mitophagy defects lead to the accumulation of damaged mitochondria, energy deprivation, inflammation, and eventually neuronal loss[2, 11, 12, 21]. Hence, compromised mitophagy could contribute significantly to AD pathology. We next examined whether activation of neuronal mitophagy through pharmacological and genetic interventions would affect AD pathogenesis. We established an *in vivo* drug-screening platform using *C. elegans* to identify potent neuronal mitophagy inducers, using a z-score standard as defined elsewhere[22]. Two different methods were used to detect neuronal mitophagy *in vivo*[10, 23]. First, we generated transgenic animals expressing a pan-neuronal mitochondria-targeted Rosella biosensor (mtRosella) with a GFP variant sensitive to the acidic environment of the lysosomal lumen fused to the pH-insensitive DsRed. We tested nematodes carrying neuronal mtRosella under normal and mitophagy-inducing conditions to validate this approach. Under normal conditions, both GFP and DsRed events were present in the neurons of WT nematodes (Supp. Fig. 2). Supplementation with NAD^+ precursor, such as nicotinamide mononucleotide (NMN), is known to induce mitophagy[12, 21, 24, 25]. Indeed, NMN supplementation resulted in decreased GFP/DsRed ratio of mtRosella fluorescence, indicating mitophagy stimulation (Fig. 2a and Supplementary Fig. 2). We then generated transgenic nematodes expressing the DCT-1 mitophagy receptor fused with GFP together with the autophagosomal marker LGG-1 fused with DsRed in neurons, and scored for co-localization events in response to NMN treatment. Similar to mtRosella, NMN promotes co-localization of DCT-1 and the LGG-1-labelled autophagosomes, indicating neuronal mitophagy elevation (Fig. 2b, c). Next, we tested a panel of compounds using our in-house small compound library as well as known autophagy/mitophagy inducers. This screen identified two potent neuronal mitophagy-inducing agents, urolithin A (UA; a small natural compound prominent in pomegranate that induces mitophagy in muscles[26]), and actinonin (AC; an antibiotic that induces *in vitro* mitophagy via a specific mitochondrial ribosomal and RNA decay pathway[27]) (Fig. 2a-c). To investigate the molecular mechanisms by which UA and AC induce neuronal mitophagy, we treated human neuronal SH-SY5Y cells with UA and AC, respectively, at doses ranging from 10-100 μM. UA increased the protein levels of a series of

mitophagy-related proteins, including F-PINK1, Parkin, Beclin1, Bcl2L13, AMBRA1, and p-ULK1(S^{555}) (Supplementary Fig. 3a). *In vivo,* UA increased F-PINK1 in an APP/PS1 mouse model (Supplementary Fig. 3b). AC exhibited very similar effects as UA (Supplementary Fig. 3a, b). Consistently, in WT nematodes, NMN, UA, and AC-induced neuronal mitophagy was dependent upon key mitophagy genes, *dct-1*, *pdr-1*, and *pink-1* (Fig. 2d and Supplementary Fig. 2). Altogether, our data suggest that NMN, UA, and AC induce robust neuronal mitophagy through the evolutionary conserved mitophagy machinery.

To determine the respective contribution of mitophagy and the more general macro-autophagy in our study, we compared doses of NMN (5 mM), UA (0.1 mM) and AC (1 mM), which we found to induce robust neuronal mitophagy (Fig. 2a-c). Under these conditions, we found no detectable changes in macro-autophagy. NMN (5 mM), UA (0.1 mM), and AC (1 mM) did not induce neuronal macro-autophagy in nematodes expressing autophagosomal protein LGG-1 fused with either GFP or DsRed (Supplementary Fig. 4a, b). We examined additional autophagy markers, such as LGG-1, LGG-2 and ATG-18/WIPI, fused with GFP upon NMN (5 mM), UA (0.1 mM) and AC (1 mM) supplementation in several tissues and found that general macro-autophagy was not induced in nematode's embryos, in intestinal, muscle and neuronal cells (Supplementary Fig. 4c-h). In conclusion, the optimized doses of NMN (5 mM), UA (0.1 mM) and AC (1 mM) specifically induce mitophagy, not macro-autophagy, in nematodes.

To investigate the contribution of neuronal mitophagy to AD pathophysiology, we took advantage of the already established models of AD in *C. elegans*[28,29]. Transgenic nematodes expressing pan-neuronal human $A\beta_{1-42}$ (CL2355) protein displayed defective energy metabolism defined by a lower oxygen consumption rate and reduced mitophagy under normal and stress (paraquat treatment) conditions (Fig. 2e-g, and Supplementary Fig. 3c). Progressive memory impairment is the most common symptom in AD patients[2, 30], and we therefore evaluated memory in the AD *C. elegans* models using an aversive olfactory learning chemotaxis assay (a negative value correlates with hungry-driven chemotaxis-related memory)[31]. Transgenic nematodes expressing $A\beta_{1-42}$ (CL2355) showed severe cognitive defects (Fig. 2h). Mitophagy induction with NMN, UA, or AC improved the memory of transgenic nematodes (CL2355) without influencing the memory of WT animals (Fig. 2i). To elucidate the mechanism by which mitophagy enables memory improvement, and to exclude off-target responses, we examined the associative memory of mitophagy deficient nematodes expressing mutant human $A\beta_{1-42}$. We generated three mitophagy mutant Aβ strains, *pink-1(tm1779)*;CL2355, *pdr-1(gk488)*;CL2355, and *dct-1(tm376)*;CL2355. Interestingly, depletion of PINK1 and PDR-1 (the nematode PINK1 and Parkin homologues) abolished the beneficial effects of UA and AC, whereas DCT-1 (the nematode BNIP3 and NIX/BNIP3L homologue) was dispensable (Supplementary Fig. 5a-d). The neuronal mitophagy induction in response to NMN, UA or AC supplementation required PINK1 and PDR-1, while the NMN-induced memory increase was dependent on DCT-1 function (Supplementary Fig. 5). This could be explained by the previously reported direct elevation of DCT-1 protein levels upon NMN treatment through the NAD^+/SIR2.1-DAF-16 pathway[12]. Additionally, UA reduced whole body Aβ levels in the CL2355 nematodes (Fig. 2j). Collectively, these findings indicate that compromised mitophagy, combined with excessive mitochondrial dysfunction contributes to a chemotaxis defect in AD nematodes. Pharmacological

stimulation of mitophagy improved the chemotactic index in transgenic $A\beta_{1-42}$ nematodes.

Restoration of neuronal mitophagy ameliorates cognitive decline and Aβ pathology in the APP/PS1 mouse model

To investigate the protective role of mitophagy against memory loss and its conservation across species, we monitored the effects of UA and AC in the APP/PS1 transgenic mouse model of AD. Transgenic AD mice were treated orally with UA (200 mg/kg/day) or AC (30 mg/kg/day) for 2 months and subsequently examined for behavioral and molecular endpoints. In congruent with the *C. elegans* results, EM analysis indicated that UA and AC administration stimulated mitophagy and promoted the elimination of defective mitochondria in the hippocampus of AD mice (Fig. 3a, b and Supplementary Fig. 6a). UA and AC also normalized mitochondrial morphology and size in the hippocampus of AD mice (Supplementary Fig. 6b). We further verified the improvement of mitophagy and mitochondrial metabolism in isolated hippocampal neurons from the 2-month UA and AC treated AD mice (Supplementary Fig. 6c-e). Using the classical Morris water maze test, both UA and AC greatly improved learning and memory retention in the AD mice with no difference in swimming speed between groups (Fig. 3c-e, and Supplementary Fig. 7a-b). The treatments normalized memory retention in the AD mice to that of WT mice (Fig. 3d-e). Mitophagy stimulation also improved spatial memory in the Y-maze spontaneous alternation behavioral test (Supplementary Fig. 7c). Several common features of AD pathology, including insoluble levels of $A\beta_{1-42}$, $A\beta_{1-40}$ and extracellular Aβ plaque burden (Fig. 3f-i) were diminished upon UA and AC treatment. While astrocytic activation, measured by GFAP levels, was increased in the vehicle-treated AD mice compared with vehicle-treated WT mice, UA or AC did not reduce the GFAP signal in the AD mice (Fig. 3i, and Supplementary Fig. 7d). We also analyzed the impact of the mitophagy inducing compounds on prefrontal cortex (PFC) of WT and AD mice. Supplementation with UA or AC resulted in the reduction of soluble $A\beta_{1-42}$ and $A\beta_{1-40}$ whereas insoluble forms remained unchanged (with a trend towards decrease) in PFC of AD mice (Supplementary Fig. 7e, f). Consistently, UA or AC promoted mitophagy eliminating damaged mitochondria and mitochondrial ROS levels in the PFC region of the AD mice (Supplementary Fig. 6f-h). To further investigate whether mitophagy induction indeed improves mitochondrial function in AD, we performed oxygen consumption rate (OCR) evaluation in the APOE4/E4 iPSC-derived neurons. UA (24 h) treatment significantly increased maximal OCR of the APOE4/E4 neurons, compatible to that of WT (veh.) neurons (Supplementary Fig. 6i). We confirmed that mitophagy induction increased OCR and reduced mitochondrial ROS in the $A\beta_{1-42}$(CL2355) worms (Supplementary Fig. 6j-l). Collectively, these findings in transgenic nematodes, iPSC-derived neurons and mouse models of AD suggest a conserved neuroprotective role of mitophagy across species against AD pathology and cognitive deficits.

To obtain a systematic unbiased overview of how mitophagy induction affects memory-related neuronal functions in AD, we performed genome-wide transcriptomic analysis of hippocampal tissue from WT and AD mice with or without UA treatment. Heat map clustering analysis of differentially expressed genes indicated that UA restores the transcriptomic profile of AD transgenic mice towards that of WT mice (Fig. 3j). Consistent with previous reports in AD, gene-set enrichment analysis of the AD (veh.) mice revealed major changes in expression level of genes associated with inflammation and neuronal function (Supplementary Fig. 8)[2, 30]. For example, *Gabra2*

(involved in GABAergic neurotransmission and Aβ clearance), *Lrrtm4* (involved in excitatory synapse development), *Slitrk1* (participates in synapse formation), and *Lgi2* (involved in synapse remodeling) were downregulated in the AD (veh.) mice, however UA treatment increased the mRNA expression of these genes (Supplementary Fig. 8a). Further pathway analysis supports that UA treatment upregulated multiple signaling pathways related to neuronal protection and memory benefits, including ATP biosynthesis, GABA A receptor activity, synapse and neuropeptide activities among others, whereas it inhibited inflammatory responses (Fig. 3k, Supplementary Fig. 8b and Supplementary Table 2). Notably, UA and AC significantly increased synaptophysin levels by over 3.5-fold, indicating an increase in synapse number (Supplementary Fig. 7g). Because synaptic failure is the major driver of memory loss in AD[32], our results suggest that mitophagy inhibits memory loss in AD mice through the maintenance of synapses, in addition to neuronal function.

Restoration of neuronal mitophagy enhances phagocytic efficiency of microglia and mitigates neuroinflammation

Aβ plaque formation is the consequence of an imbalance between Aβ clearance and its production from proteolytic cleavage of amyloid precursor protein (APP)[30]. Supplementation with UA did not alter the levels of APP cleavage intermediates, including N- and C-terminal fragments, in hippocampus of transgenic AD animals (Supplementary Fig. 7h). AC treatment reduced CTFs while no significant effect on the APP NTF (Supplementary Fig. 7h). Thus, we investigated whether there was enhanced Aβ plaque removal upon pharmacological mitophagy induction. Microglia are the primary immune and phagocytic cells of the central nervous system. They play a crucial role in the clearance of extraneuronal Aβ plaques, which impact AD development and progression[30, 33]. Therefore, we evaluated whether mitophagy stimulation influences microglia activity, and whether increased microglial activity could enhance the removal of Aβ plaques. Indeed, we observed increased engulfment of Aβ plaques by microglia in response to AC and UA treatment (Fig. 4a and Supplementary Fig. 7j). UA (but not AC) supplementation resulted in an increased microglial population (Supplementary Fig. 7j). Further, UA and AC-treated animals displayed a decreased number and length of microglial processes highlighting their shift towards a phagocytic state (Supplementary Fig. 7j)[30]. In accord with this, mitophagy induction increased the expression of engulfment associated protein CD68, microglia-enriched transcriptional regulator IRF7, and a microglia proliferation marker CSF2RA, without changing the levels of osteopontin, a cell adhesion and migration regulator (Fig. 4b and quantification in Supplementary Fig. 7g). Mitophagy in the microglia cells was decreased by 60% in the hippocampus of AD mice compared to WT (Fig. 4c), and there were more damaged mitochondria in AD microglia than in WT (Fig. 4d). UA and AC treatments normalized mitophagy in the AD microglia and decreased the extent of mitochondrial damage (Fig. 4c, d, and Supplementary Fig. 7i). Phagocytosis requires large amounts of energy, which is mainly derived from mitochondria. Therefore, our results suggest that mitophagy induction increases the efficiency of phagocytosis of Aβ plaques by microglia through balanced mitochondrial homeostasis providing the required energy.

While essential for the removal of Aβ plaques, microglia also contribute to local neuroinflammation that causes neurotoxicity and disease progression[30, 33]. Microglia often exist in an activated state and produce pro-inflammatory cytokines in AD mice[34]. Therefore, we examined whether mitophagy-inducing compounds affect the levels of

neuroinflammation in the APP/PS1 AD mice. UA and AC reduced the protein levels of several key pro-inflammatory cytokines including IL-6 and TNF-α (Fig. 4e, f). The IL-10 anti-inflammatory cytokine was recently found to promote mitophagy in primary macrophages[35]. Interestingly, treatment with UA increased IL-10 levels in hippocampal tissue by 4-fold (Fig. 4g). The inflammation data were generated using the brain tissues where the interpretation of a direct role of mitophagy induction in the reduction of microglia-related inflammation was limited. To address this concern, we isolated microglia from the brain tissues of the WT and the APP/PS1 mice, followed by siRNA knock down of *Pink1* in the AD microglia. In this pure microglia culture system, depletion of *Pink1* increased the expression of the inflammatory marker TNF-α and almost completely eliminated UA-induced inhibition of TNF-α, with a similar non-significant trend for IL-10 (Fig. 4h, i). To investigate the intrinsic mechanisms of this mitophagy enhancement and inflammation, we examined the activity of the NLRP3 inflammasome, which was reported to be activated in AD mice, and whose activation promotes AD[36]. We found elevated expression of NLRP3 and increased expression of cleaved-Caspase1 in the brain tissues of AD mice, indicating an increase in the activity of NLRP3. In UA-treated APP/PS1 mice, the expression and activity of NLRP3 were reduced as evidenced by lower level of its downstream proteins, including cleaved-Caspase1, pro-IL1β, and active IL1β (Fig. 4j). These findings, combined with the reduced insoluble $A\beta_{1-42}$ and $A\beta_{1-40}$ protein levels noted above in the hippocampus of transgenic APP/PS1 AD animals, indicate that mitophagy stimulation enhances phagocytic efficiency of microglia, and at the same time mitigates a NLRP3/caspase-1-dependent neuro-inflammation.

Restoration of neuronal mitophagy ameliorates p-Tau pathology and cognitive deficits in AD across species

Amyloid plaques and neurofibrillary tangles are hallmark features of AD pathology. In AD transgenic mice, abnormal accumulation of Aβ peptides instigate the formation of extracellular amyloid plaques, whereas intra-neuronal aggregation of p-Tau proteins generates neurotoxic Tau tangles leading to defective axonal transport of mitochondria and synaptotoxicity[6, 37]. Several p-Tau sites, such as Thr^{181}, Ser^{202}/Thr^{205}, Thr^{231} and Ser^{262} are considered possible clinical biomarkers of AD in human patients[37, 38]. Thus, we examined whether mitophagy-inducing compounds regulate p-Tau. UA treatment inhibits phosphorylation of many of the p-Tau sites (Fig. 5a and Supplementary Fig. 9a). UA inhibited p-Tau in a mitophagy-dependent manner as the effect was diminished in PINK1 knockdown and ULK1 knockdown cells (Fig. 5b). We then investigated the effects of mitophagy induction in a Tau worm model (BR5270) with pan-neuronal expression of the pro-aggregating F3ΔK280 Tau fragment[28]. This Tau (BR5270) nematode strain shows severe mitochondrial dysfunction as indicated by 70% decrease of its basal OCR and loss of reserve capacity relative to WT (Fig. 5c, d). Moreover, both basal and stress-induced (paraquat treatment) mitophagy events were decreased in the Tau (BR5270) nematodes (Fig. 5e, f). Importantly, memory loss in the Tau (BR5270) nematodes was restored by pharmacological mitophagy stimulation (Fig. 5g, h). To verify that memory retention is dependent on mitophagy in AD, we generated three mitophagy mutant Tau strains, *pink-1(tm1779)*;BR5270, *pdr-1(gk488)*;BR5270, and *dct-1(tm376)*;BR5270. While NMN-induced memory retention in the BR5270 nematodes was dependent on PINK1, PDR-1 and DCT-1, UA was dependent on PINK1 and PDR-1, and AC was only PINK1 dependent (Supplementary Fig. 9b-e). In addition, UA-induced mitophagy induction reduced mitochondrial ROS in the BR5270 worms (Supplementary Fig. 6l).

To test the conserved beneficial role of mitophagy induction in p-Tau, we next performed a one-month UA treatment protocol in the 3xTgAD mice. We first performed the contextual and cued fear conditioning test to assess learning and memory of an association between environmental cues and aversive experiences[39]. While there was no difference in context freezing time, UA affected a trend of increased cued freezing time in the 3xTgAD mice (Fig. 5i, j). Intriguingly, both object recognition and Y-maze tests indicated normalization of performance by UA in the 3xTgAD mice to that of WT (veh.) mice (Fig. 5 k, l). At the molecular level, UA showed strong p-Tau inhibition activity, at sites including Thr^{181}, Ser^{202}/Thr^{205}, Ser^{262} (Fig. 5m), similar to its function in the Tau-overexpressed human SH-SY5Y cells. Because sex is a biological variable in AD[40], we investigated any sex difference in the responses to the mitophagy inducers in both the APP/PS1 and the 3xTgAD mice. While UA appeared to be more potent towards the male APP/PS1 mice than females, it showed similar effects in male and female 3xTgAD mice (Supplementary Fig. 10). Due to small group sizes of mice with each gender, future studies are necessary to gain full insight into the sex differences. Altogether, our observations strongly indicate that mitophagy induction inhibits phosphorylation of Tau protein, resulting in memory improvement in both *C. elegans* and mouse models of taupathies.

Discussion

Our cross-species analysis provides evidence that mitophagy defects have a critical role in AD development and progression. Mitochondrial dysfunction is a common pathological feature and contributes to neurodegeneration in both transgenic animal models and in human AD patients[2, 41]. Impairment of mitochondrial proteostasis and exhaustion of the mitochondrial unfolded protein response (UPR^{mt}) have been implicated in the pathogenesis of AD[4]. Diverse changes in mitophagy in AD in different systems have been reported[42, 43]. Our results suggest that impaired initiation of mitochondrial selective autophagy, due to decreased levels of activated mitophagic proteins, such as p-TBK1 and p-ULK1, result in the accumulation of dysfunctional mitochondria and impaired cellular energy metabolism. We demonstrate that defective mitophagy, which can be caused by both $A\beta_{1-42}$ and p-Tau, is a major element of AD progression and memory loss in a manner that is conserved from *C. elegans* and mice to humans. Defective mitophagy and mitochondrial dysfunction hampers ATP production, which induces AMPK activation (p-AMPK). AMPK activation often leads to excessive mitochondrial fission[14], and further reduces ATP production in a vicious cycle. Hyper-activation of p-AMPK induces Tau phosphorylation which is critical of the synaptotoxic effects of $A\beta_{1-42}$ oligomers[6]. Interestingly, several reports show $A\beta_{1-42}$ oligomers can activate AMPK in a CAMKK2-dependent manner in neurons[44, 45], which may further exacerbate cellular levels of p-Tau. Further studies to uncouple the interconnected sophisticated roles between defective mitophagy, AMPK, p-Tau and Aβ in AD etiology and progression are necessary. A working model is proposed (Supplementary Fig. 11).

Our new findings extends the 'AD mitochondrial cascade hypothesis' [2, 41] through the linkage of defective mitophagy to damaged mitochondria. First, we show Aβ inhibits mitophagy while mitophagy induction reduces Aβ. Second, we show that tau impairs mitophagy while mitophagy inhibits several common p-Tau sites. However, they also raise many important questions, such as a) the chronological sequence of defective

mitophagy, Aβ, and Tau tangles; b) whether defective mitophagy and AD pathologies exacerbate one another; and c) whether any sex differences of mitophagy exist in AD patients in view of the prevalence of AD and other dementias is higher in women than in men[40]. While it is difficult to address these questions with the current transgenic AD animal models, novel animal models more similar to human AD, as well as human longitudinal studies, may provide insight.

In mammals, there are multiple mitophagy pathways suggesting that dysfunction of one can be compensated by others[2, 16]. In AD, defects in mitophagy (as evaluated in this study) and autophagy[19] may occur at different steps within these pathways. We found that three distinct pharmacological approaches were effective in counteracting AD pathogenic processes and ameliorating cognitive impairment suggesting a potential for clinical interventions that enhance mitophagy via different mechanisms. For example, BNIP3L/NIX/DCT-1 serves as a mitophagy receptor mediating the clearance of damaged mitochondria and assures stress resistance and healthy aging[2, 10]. Interestingly, some AD patients display reduced levels of BNIP3L/NIX (indicating mitophagy defects). Although a NMN-induced memory enhancement depends on DCT-1 functionality, AC- and UA-induced memory improvement was independent of DCT-1, and can thus be beneficial when BNIP3L/NIX function is compromised. Our findings provide a pharmacological approach to optimize and overcome deficits in different mitophagy pathways and thereby to ameliorate cognitive impairments with both Aβ and Tau pathologies.

An interconnected network between neurons and supporting glial cells, including microglia, maintains brain homeostasis. Our findings suggest that the accumulation of damaged mitochondria and compromised mitophagy influences not only neurons but also microglia in AD. Microglia play a pivotal role in the removal of neurotoxic proteinaceous components and simultaneously release pro- and anti-inflammatory cytokines regulating immune responses[46]. In the APP/PS1 mice, we show accumulation of damaged mitochondria and defective mitophagy in microglia, leading to impaired efficacy of phagocytic clearance of Aβ plaques. Hence, mitophagy restoration promotes the elimination of dysfunctional organelles and enhance microglial phagocytic capacity (Supplementary Fig. 11). Importantly, microglia exhibit confounding roles in AD, including protective functions (e.g., phagocytosis)[30, 33] and detrimental effects (e.g., release of inflammatory cytokines and related cross-seeding of Aβ)[46, 47]. Our study unveils a previously unexplored function of mitophagy that coordinates both phagocytosis and anti-inflammation in microglia. At the molecular level, both PINK1[48] and Parkin[49] have been shown to play important roles in the improvement of mitochondrial function and the elimination of intracellular Aβ in AD mice. Our study extends the importance of the PINK1-dependent pathway to the elimination of pro-inflammatory cytokines by the AD microglia. More broadly, by providing evidence of a protective role for mitophagy in neurons and microglia, the current study raises the possibility that mitophagy induction is also beneficial to other glial cells as well as other non-neuronal cells. Emerging evidence suggests that AD affects not only the brain but also peripheral tissues[50]. Thus, targeting mitochondrial quality maintenance at both neuronal and organismal levels may be a promising therapeutic approach.

Accession codes

The microarray GEO accession number for the data reported in this paper is GSE111737.

Acknowledgements

We thank R. Legouis (Institut de Biologie Intégrative de la Cellule) for *C. elegans* strain expressing GFP::LGG-2. Some nematode strains used in this work were provided by the Caenorhabditis Genetics Center, which is funded by the National Center for Research Resources of the National Institutes of Health, and S. Mitani (National Bioresource Project) in Japan. We thank A. Fire for plasmid vectors. We thank S. Cordonnier, H. Kassahun, J. Tian, W.B. Iser, M.A. Wilson, D. Figueroa, E. Fivenson, Q.P. Lu for experiments on *C. elegans* and mice; K. Marosi and T.G. Demarest for Seahorse studies; M. Kang, Y.Q. Zhang, E. Lehrmann and K. Becker for array data analysis; A. Pasparaki for technical support with experiments. We thank N.F. Borhan for reading the paper. This research was supported by the Intramural Research Program of the NIH, the National Institute on Aging (V.A.B.), the HELSE SøR-ØST (E.F.F., #2017056 and H.N. # 275911), The Research Council of Norway (E.F.F., #262175 and #277813), two NIA Intra-laboratory grants (2016, 2017 to E.F.F. and V.A.B.), the European Research Council (ERC – GA695190 – MANNA, ERC – GA737599 – NeuronAgeScreen), the European Commission Framework Programmes and the Greek Ministry of Education (N.T) and the Thon foundation (V.A.B.). K.P. is supported by an AXA Research Fund post-doctoral long-term fellowship.

Author Contributions

E.F.F., Y.H., K.P. and V.A.B. designed experiments. E.F.F. performed microarray and D.L.C. analyzed the data. E.F.F., Y.H., D.C., and J.S.K. performed western blot. E.F.F., J.S.K., and M.H. did the seahorse experiments. Y.H., J.S.K., B.Y., and S. L. performed animal treatment, histology, IHC, and ELISA experiments. K.P., N.T., E.F.F., J.S.K., and X.D. performed *C. elegans* experiments. B.A.A., P.R. and M.Z.C. performed stem cell experiment. E.F.F., Y.H., K.P., D.L.C., M.A., N.H.G., T.F., H.N., M.P.M., and V.A.B. wrote the manuscript.

Competing interests

E.F.F., V.A.B., and H.N., have CRADA arrangements with ChromaDex.

References

1. Scheibye-Knudsen, M., Fang, E.F., Croteau, D.L., Wilson, D.M., 3rd & Bohr, V.A. Protecting the mitochondrial powerhouse. *Trends Cell Biol* **25**, 158-170 (2015).
2. Kerr, J.S. *et al.* Mitophagy and Alzheimer's Disease: Cellular and Molecular Mechanisms. *Trends Neurosci* **40**, 151-166 (2017).
3. Lustbader, J.W. *et al.* ABAD directly links Abeta to mitochondrial toxicity in Alzheimer's disease. *Science* **304**, 448-452 (2004).
4. Sorrentino, V. *et al.* Enhancing mitochondrial proteostasis reduces amyloid-beta proteotoxicity. *Nature* (2017).
5. Devi, L., Prabhu, B.M., Galati, D.F., Avadhani, N.G. & Anandatheerthavarada, H.K. Accumulation of amyloid precursor protein in the mitochondrial import channels of human Alzheimer's disease brain is associated with mitochondrial dysfunction. *J Neurosci* **26**, 9057-9068 (2006).
6. Mairet-Coello, G. *et al.* The CAMKK2-AMPK kinase pathway mediates the synaptotoxic effects of Abeta oligomers through Tau phosphorylation. *Neuron* **78**, 94-108 (2013).
7. Vossel, K.A. *et al.* Tau reduction prevents Abeta-induced defects in axonal transport. *Science* **330**, 198 (2010).
8. Mandelkow, E.M., Stamer, K., Vogel, R., Thies, E. & Mandelkow, E. Clogging of axons by tau, inhibition of axonal traffic and starvation of synapses. *Neurobiol Aging* **24**, 1079-1085 (2003).
9. Dixit, R., Ross, J.L., Goldman, Y.E. & Holzbaur, E.L. Differential regulation of dynein and kinesin motor proteins by tau. *Science* **319**, 1086-1089 (2008).
10. Palikaras, K., Lionaki, E. & Tavernarakis, N. Coordination of mitophagy and mitochondrial biogenesis during ageing in C. elegans. *Nature* **521**, 525-528 (2015).
11. Fang, E.F. *et al.* Defective mitophagy in XPA via PARP-1 hyperactivation and NAD(+)/SIRT1 reduction. *Cell* **157**, 882-896 (2014).
12. Fang, E.F. *et al.* NAD+ Replenishment Improves Lifespan and Healthspan in Ataxia Telangiectasia Models via Mitophagy and DNA Repair. *Cell Metab* **24**, 566-581 (2016).
13. Canto, C. *et al.* AMPK regulates energy expenditure by modulating NAD+ metabolism and SIRT1 activity. *Nature* **458**, 1056-1060 (2009).
14. Toyama, E.Q. *et al.* Metabolism. AMP-activated protein kinase mediates mitochondrial fission in response to energy stress. *Science* **351**, 275-281 (2016).
15. Egan, D.F. *et al.* Phosphorylation of ULK1 (hATG1) by AMP-activated protein kinase connects energy sensing to mitophagy. *Science* **331**, 456-461 (2011).
16. Lazarou, M. *et al.* The ubiquitin kinase PINK1 recruits autophagy receptors to induce mitophagy. *Nature* **524**, 309-314 (2015).
17. Handel, A.E. *et al.* Assessing similarity to primary tissue and cortical layer identity in induced pluripotent stem cell-derived cortical neurons through single-cell transcriptomics. *Hum Mol Genet* **25**, 989-1000 (2016).
18. Shi, Y., Kirwan, P. & Livesey, F.J. Directed differentiation of human pluripotent stem cells to cerebral cortex neurons and neural networks. *Nat Protoc* **7**, 1836-1846 (2012).
19. Menzies, F.M., Fleming, A. & Rubinsztein, D.C. Compromised autophagy and neurodegenerative diseases. *Nat Rev Neurosci* **16**, 345-357 (2015).
20. Kimura, S., Noda, T. & Yoshimori, T. Dissection of the autophagosome maturation process by a novel reporter protein, tandem fluorescent-tagged LC3. *Autophagy* **3**, 452-460 (2007).
21. Fivenson, E.M. *et al.* Mitophagy in neurodegeneration and aging. *Neurochem Int* **109**, 202-209 (2017).
22. Zhang, J.H., Chung, T.D. & Oldenburg, K.R. A Simple Statistical Parameter for Use in Evaluation and Validation of High Throughput Screening Assays. *J Biomol Screen* **4**, 67-73 (1999).
23. Fang, E.F. *et al.* In Vitro and In Vivo Detection of Mitophagy in Human Cells, C. Elegans, and Mice. *J Vis Exp* (2017).
24. Aman, Y., Qiu, Y., Tao, J. & Fang, E.F. Therapeutic potential of boosting NAD+ in aging and age-related diseases. *Translational Medicine of Aging* **1**, https://doi.org/10.1016/j.tma.2018.1008.1003 (2018).
25. Fang, E.F. *et al.* NAD(+) in Aging: Molecular Mechanisms and Translational Implications. *Trends in Molecular Medicine* **23**, 899-916 (2017).
26. Ryu, D. *et al.* Urolithin A induces mitophagy and prolongs lifespan in C. elegans and increases muscle function in rodents. *Nat Med* **22**, 879-888 (2016).
27. Sun, N. *et al.* Measuring In Vivo Mitophagy. *Mol Cell* **60**, 685-696 (2015).

28. Fatouros, C. *et al.* Inhibition of tau aggregation in a novel Caenorhabditis elegans model of tauopathy mitigates proteotoxicity. *Hum Mol Genet* **21**, 3587-3603 (2012).
29. Lublin, A.L. & Link, C.D. Alzheimer's disease drug discovery: in vivo screening using Caenorhabditis elegans as a model for beta-amyloid peptide-induced toxicity. *Drug Discov Today Technol* **10**, e115-119 (2013).
30. Iaccarino, H.F. *et al.* Gamma frequency entrainment attenuates amyloid load and modifies microglia. *Nature* **540**, 230-235 (2016).
31. Voglis, G. & Tavernarakis, N. A synaptic DEG/ENaC ion channel mediates learning in C. elegans by facilitating dopamine signalling. *EMBO J* **27**, 3288-3299 (2008).
32. Selkoe, D.J. Alzheimer's disease is a synaptic failure. *Science* **298**, 789-791 (2002).
33. Keren-Shaul, H. *et al.* A Unique Microglia Type Associated with Restricting Development of Alzheimer's Disease. *Cell* **169**, 1276-1290 e1217 (2017).
34. Babcock, A.A. *et al.* Cytokine-producing microglia have an altered beta-amyloid load in aged APP/PS1 Tg mice. *Brain Behav Immun* **48**, 86-101 (2015).
35. Ip, W.K.E., Hoshi, N., Shouval, D.S., Snapper, S. & Medzhitov, R. Anti-inflammatory effect of IL-10 mediated by metabolic reprogramming of macrophages. *Science* **356**, 513-519 (2017).
36. Heneka, M.T. *et al.* NLRP3 is activated in Alzheimer's disease and contributes to pathology in APP/PS1 mice. *Nature* **493**, 674-678 (2013).
37. Spillantini, M.G. & Goedert, M. Tau pathology and neurodegeneration. *Lancet Neurol* **12**, 609-622 (2013).
38. Hanger, D.P. *et al.* Novel phosphorylation sites in tau from Alzheimer brain support a role for casein kinase 1 in disease pathogenesis. *Journal of Biological Chemistry* **282**, 23645-23654 (2007).
39. Hou, Y. *et al.* NAD(+) supplementation normalizes key Alzheimer's features and DNA damage responses in a new AD mouse model with introduced DNA repair deficiency. *Proc Natl Acad Sci U S A* **115**, E1876-E1885 (2018).
40. Mazure, C.M. & Swendsen, J. Sex differences in Alzheimer's disease and other dementias. *Lancet Neurol* **15**, 451-452 (2016).
41. Swerdlow, R.H., Burns, J.M. & Khan, S.M. The Alzheimer's disease mitochondrial cascade hypothesis: progress and perspectives. *Biochim Biophys Acta* **1842**, 1219-1231 (2014).
42. Martin-Maestro, P. *et al.* Mitophagy Failure in Fibroblasts and iPSC-Derived Neurons of Alzheimer's Disease-Associated Presenilin 1 Mutation. *Front Mol Neurosci* **10**, 291 (2017).
43. Ye, X., Sun, X., Starovoytov, V. & Cai, Q. Parkin-mediated mitophagy in mutant hAPP neurons and Alzheimer's disease patient brains. *Hum Mol Genet* **24**, 2938-2951 (2015).
44. Thornton, C., Bright, N.J., Sastre, M., Muckett, P.J. & Carling, D. AMP-activated protein kinase (AMPK) is a tau kinase, activated in response to amyloid beta-peptide exposure. *Biochem J* **434**, 503-512 (2011).
45. Yoon, S.O. *et al.* JNK3 perpetuates metabolic stress induced by Abeta peptides. *Neuron* **75**, 824-837 (2012).
46. Sarlus, H. & Heneka, M.T. Microglia in Alzheimer's disease. *J Clin Invest* **127**, 3240-3249 (2017).
47. Venegas, C. *et al.* Microglia-derived ASC specks cross-seed amyloid-beta in Alzheimer's disease. *Nature* **552**, 355-361 (2017).
48. Du, F. *et al.* PINK1 signalling rescues amyloid pathology and mitochondrial dysfunction in Alzheimer's disease. *Brain* **140**, 3233-3251 (2017).
49. Khandelwal, P.J., Herman, A.M., Hoe, H.S., Rebeck, G.W. & Moussa, C.E. Parkin mediates beclin-dependent autophagic clearance of defective mitochondria and ubiquitinated Abeta in AD models. *Hum Mol Genet* **20**, 2091-2102 (2011).
50. Bu, X.L. *et al.* Blood-derived amyloid-beta protein induces Alzheimer's disease pathologies. *Mol Psychiatry* (2017).

Figure Legends

Figure 1. Mitochondrial dysfunction and defective mitophagy in human patient brain samples and AD patient iPSC-derived cultured neurons. a, Quantification of mitochondrial parameters from EM images in postmortem human hippocampal tissues from AD patients and age-matched healthy controls; n= 300 mitochondria from 7 AD patients or 203 mitochondria from 7 healthy control individuals. Center value represents mean and error bars represent s.e.m. (***p<0.001; two-sided Student's t test). **b**, A representative set of EM figures. **c**, Relative levels of proteins implicated in the AMPK pathway in postmortem human hippocampal tissues from AD patients and age-matched healthy controls. **d**, Quantification of the co-localization of the mitochondrial protein TOMM20 and the lysosomal protein LAMP2 protein using immunohistochemistry. Center value represents mean and error bars represent s.e.m. (n = 9 random fields from 3 AD patients or 3 healthy control individuals; ***p<0.001; two-sided Student's t test). **e**, Quantification of mitophagy-like events using EM images in postmortem human hippocampal tissues between AD patients and age-matched healthy controls. Center value represents mean and error bars represent s.e.m. (n = 9 random fields from 3 AD patients or 3 healthy control individuals; ***p<0.001; two-sided Student's t test). **f**, Changes of designated mitophagy proteins in postmortem human hippocampal tissues from AD patients and age-matched healthy controls (n = 7 individuals for both the AD group and the healthy control group). **g**, Representative images of iPSC-derived neurons from an APP patient, an APOE4 patient and healthy age-matched control cell line (28-day differentiation). **h**, Immunofluorescence microscopy for DAPI (nuclear staining), MAP2 (staining of dendrites), and Tuj1 (staining of Neuron-specific class III beta-tubulin) in the control line neurons, with scale bars 50μm. **i**, Immunofluorescence microscopy for DAPI (nuclear staining) and BRN2 (cortical upper layer marker) in the control line neurons, with scale bars 50μm. **j**, Levels of mitophagy-related proteins in iPSC-derived neurons in three iPSC cell lines. For Fig. 1c, f, g, h, i, j, at least 3 experiments were repeated independently with similar results. Full scans of all the blots are in Supplementary Note.

Figure 2. Mitophagy induction restores memory in Aβ_{1-42} *C. elegans* model of AD. **a**, Transgenic animals expressing the mtRosella biosensor in neuronal cells were treated with nicotinamide mononucleotide (NMN), urolithin A (UA) and actinonin (AC). Relative levels of neuronal mitophagy are expressed as the ratio between pH-sensitive GFP fluorescence intensity and pH-insensitive DsRed fluorescence intensity. Center value represents mean and error bars represent s.e.m. (n = 35 nematodes/group; ***p<0.001; one-way ANOVA followed by *Sidak*'s multiple comparisons test). **b**, Transgenic nematodes were treated with NMN, UA and AC. Mitophagy events were calculated by the colocalization between the autophagic marker DsRed::LGG-1 and the mitophagy receptor DCT-1::GFP in neurons. Center value represents mean and error bars represent s.e.m. (n =18-20 neurons/group as detailed in the figure; ***p<0.001; one-way ANOVA followed by *Sidak*'s multiple comparisons test). **c**, Representative images of b with scale bars 5 μm. **d**, Transgenic nematodes expressing mtRosella biosensor in neuronal cells treated with NMN, UA, and AC. Decreased GFP/DsRed ratio of mtRosella indicates neuronal mitophagy stimulation. DCT-1, PDR-1 and PINK1 were required for neuronal mitophagy induction in response to UA, NMN and AC treatment. Center value represents mean and error bars represent s.e.m. (n = 32-102 nematodes/group as detailed in the figure; n.s., p>0.05 and ***p<0.001; one-way ANOVA followed by *Sidak*'s multiple comparisons test). **e** and **f**, Nematodes

expressing $A\beta_{1-42}$ display decreased basal levels (**e**) and reserve capacity (**f**) of oxygen consumption rate (OCR). Center value represents mean and error bars represent s.e.m. (n = 3 independent experiments; ***p<0.001; two-sided Student's t test). **g**, Mitophagy events were reduced in neuronal cells of $A\beta_{1-42}$ expressing nematodes under control and oxidative stress (paraquat/para. 8 mM) conditions. Center value represents mean and error bars represent s.e.m. (n = 26-27 neurons/group as detailed in the figure; n.s., p>0.05 and ***p<0.001; one-way ANOVA followed by *Sidak*'s multiple comparisons test). **h**, Aversive conditioning (to isoamyl alcohol (IA) in the absence of food) is impaired in transgenic animals expressing $A\beta_{1-42}$ (CL2355) in neurons. Bars depict chemotaxis indices towards IA, monitored for either naïve or conditioned WT and $A\beta_{1-42}$ expressing nematodes. Center value represents mean and error bars represent s.e.m. (n = 400 nematodes/group; ***p<0.001; Two-way ANOVA followed by Tukey's multiple comparisons test). **i**, Dietary supplementation with UA, NMN or AC improves associative memory in transgenic nematodes expressing $A\beta_{1-42}$ (CL2355). Bars depict chemotaxis indices towards IA, measured for either naïve or conditioned WT and $A\beta_{1-42}$ expressing nematodes with or without UA, NMN and AC treatment. Center value represents mean and error bars represent s.e.m. (n = 400 nematodes/group; ***p<0.001; Two-way ANOVA followed by Tukey's multiple comparisons test). Experiments for the data in panels h and i were performed together and thus share the same data for the vehicle groups**. j.** UA reduces Aβ peptides in CL2355 nematodes (Day 5). Center value represents mean and error bars represent s.e.m. (n = 7 biologically independent samples in the veh. group or 8 biologically independent samples in the UA-treated group; *p<0.05; two-sided Student's t test). For all worm experiments, 2 to 4 independent experiments were performed.

Figure 3. Mitophagy induction ameliorates Aβ pathology and cognitive decline in APP/PS1 AD mice. The APP/PS1 mice were treated with UA (200 mg/kg/day) or AC (30 mg/kg/day) by daily gavage for 2 months starting from 6 months of age, and then behavioral tests were performed and brains were subjected to histological and molecular analyses. **a** and **b**, EM analysis shows that hippocampal neurons in UA- and AC-treated AD mice display increased mitophagy-like events (**a**) and removal of damaged mitochondria (**b**). For (a) and (b), center value represents mean and error bars represent s.e.m (n = 9 random fields from 3 mice; ***p<0.001; One-way ANOVA). **c**, The latencies to escape to a hidden platform in the Morris water maze during a 7 day training period. Detailed statistics: Day 3, WT vs. AD (veh), P = 0.0010, AD (veh) vs. AD (AC), P = 0.0052; day 4, WT vs. AD (veh), P = 0.0006, AD (veh) vs. AD (AC), P = 0.0317; day 5, WT vs. AD (veh), P = 0.0063; day 6, WT vs. AD (veh), P < 0.0001, AD (veh) vs. AD (UA), P = 0.0137; day 7, WT vs. AD (veh), P < 0.0001, AD (veh) vs. AD (UA), P = 0.0060 (n = 13 mice in the WT veh. group, or 11 mice in all the other groups; *p<0.05, **p<0.01, ***p<0.001; Two-way ANOVA followed by Tukey's multiple comparisons test). **d** and **e**, Further analysis of the Morris water maze test of time in target quadrant in probe trial (d), and the number of times mice passed through the platform location in probe trial (e). Center value represents mean and error bars represent s.e.m. (n = 13 mice in the WT veh. group or 11 mice in all the other groups; *p<0.05, **p<0.01; One-way ANOVA). **f** and **g**, Soluble and insoluble $A\beta_{1-42}$ and $A\beta_{1-40}$ levels in hippocampal tissues. Center value represents mean and error bars represent s.e.m. (n = 9 mice in the AD UA. group, while n = 8 mice in all the other groups; *p<0.05, **p<0.01; One-way ANOVA). **h**, The number of Aβ plaques is decreased upon UA and AC treatment in hippocampus. Center value represents mean and error bars represent s.e.m. (n = 20 random areas in ROI from 3 mice; ***p<0.001; One-way ANOVA). **i**,

Immunohistochemistry of amyloid plaques (6E10 antibody), astrocytes (GFAP antibody), and DAPI. Scale bar, 200 μm. Small figures, scale bar, 20 μm. The experiments were repeated 2 times independently with similar results. **j**, Heat map of differentially expressed genes as determined by microarray of hippocampal tissues.. **k**, Transcriptomic analysis of GO pathways between AD (UA) and AD (veh.). Error bars, ± s.e.m. For j-k, n = 5, 6, 4 mice for AD (veh.), AD (UA), and WT (veh.), respectively.

Figure 4. Mitophagy induction promotes phagocytic activity of microglia and inhibits neuronal inflammation in APP/PS1 AD mice. a, Representative images showing microglial cells engulfing or near Aβ plaques. Aβ plaques are shown in green (6E10 antibody) and microglia (anti-Iba1 antibody) are in red. **b,** Effects of UA and AC on expression level of proteins involved in microglial phagocytosis and synaptic function in hippocampus (n = 3 mice/group). Synapto., Synaptophysin; Osteo. Osteopontin. **c** and **d**, EM data show elevation of mitophagy-like events (**c**) and diminished mitochondrial damage (**d**) in response to UA and AC administration. Center value represents mean and error bars represent s.e.m. (n = 3 mice/group; **p*<0.05, ***p*<0.01, ****p*<0.001; One-way ANOVA). **e-g**, Levels of indicated cytokines were altered upon UA- and AC-induced mitophagy. Center value represents mean and error bars represent s.e.m. (n = 5 mice in WT veh., or 5 in AD veh., or 6 in AD UA, or 4 in AD AC; n.s., *p*>0.05 and **p*<0.05, ***p*<0.01, ****p*<0.001; One-way ANOVA). **h-i**, UA inhibits inflammation in microglia isolated from the APP/PS1 mice via PINK1-dependent mitophagy. The $CD11b^{+}$, $CD45^{low}$ microglial cells were isolated from brain tissues of WT and the APP/PS1 mice through a FACS sorting system. Cells were then cultured for the knocking down of *Pink1*, followed by the treatment of UA (50 μM for 24 h). Cytokines were detected using commercial ELISA kits. Center value represents mean and error bars represent s.e.m. (n = 8 mice in the WT veh. group, or 6 in the other groups; **p*<0.05; One-way ANOVA). **j**, Western blotting data showing effects of UA on the expression levels of proteins involved in NLRP3 inflammasome activity and inflammation in the cortex tissues of the mice (n = 3 mice/group). Numbers inserted were mean of the average protein level/three samples. Tissues/cells from 8 months old mice were used for the experiments. Full scans of all the blots are in Supplementary Note.

Figure 5. Mitophagy induction inhibits Tau hyperphosphorylation in human neuronal cells and enhances memory in a Tau *C. elegans* model and a 3xTgAD mouse model. a, Levels of p-Tau in human SH-SY5Y neuroblastoma cells overexpressing 2N4R, 1N4R or 2N3R Tau or empty vector, that had been treated for 24 h with either vehicle or 50 μM UA. 'S', short exposure, 'L', long exposure of the same blot. Two independent experiments performed with similar results. **b**, UA-induced inhibition of pTau at Ser^{202}/Thr^{205} is dependent on PINK1 and ULK1. Two independent experiments performed with similar results. **c** and **d**, Nematodes expressing Tau present decreased basal levels (c) and reserve capacity (d) of oxygen consumption rate (OCR). Center value represents mean and error bars represent s.e.m. (n = 3 independent experiments; ****p*<0.001; Two-sided Student's *t*-test). **e**, Mitophagy events are reduced in neurons of Tau expressing nematodes under normal and oxidative stress (paraquat/para. 8 mM) conditions. Center value represents mean and error bars represent s.e.m. (n = 30 neurons/group; n.s., *p*>0.05 and ****p*<0.001; One-way ANOVA followed by *Sidak*'s multiple comparisons). Experiments for 2g and

5e were performed together with the same WT control. **f**, Representative images of mitophagy events in WT and Tau (BR527) nematodes under normal and oxidative stress conditions (paraquat/para. 8 mM) in neurons. Co-localization of the mitophagy receptor DCT-1::GFP and the autophagosomal protein DsRed::LGG-1 indicates mitophagy events. Scale bars, 2 μm. **g**, Conditioning to isoamyl alcohol (IA) in the absence of food is impaired in transgenic nematodes expressing human Tau (BR5270) in neurons. Bars depict chemotaxis indices towards IA, monitored for either naïve or conditioned WT and Tau expressing nematodes. Center value represents mean and error bars represent s.e.m. (n = 400 nematodes/group; ***p<0.001; Two-way ANOVA followed by Tukey's multiple comparisons test).**h**, Supplementation of UA, NMN or AC improves memory in transgenic animals expressing Tau (BR5270). Bars depict chemotaxis indices towards isoamyl alcohol (IA), measured for either naïve or conditioned WT and Tau expressing nematodes with or without UA, NMN and AC treatment. Center value represents mean and error bars represent s.e.m. (n = 400 nematodes/group; ***p<0.001; Two-way ANOVA followed by Tukey's multiple comparisons test). Experiments for (g) were performed together with (h) and, thus share the same data for the vehicle group. **i-l**, One-month UA treatment improves memory performance and inhibits p-Tau in 3xTgAD mice. Thirteen-month old 3xTgAD mice were treated with UA (200 mg/kg/day) by daily gavage for 1 month. Contextual and cued fear conditioning test (i, j), object recognition test (k), and Y-maze test (l) were performed. For (i-l), center value represents mean and error bars represent s.e.m. (n = 7; *p<0.05, ***p<0.001; Two-sided Student's t-test was used for i and j while One-way ANOVA was used for k and l). **m**, Western blot was used to evaluate changes of designated p-Tau sites using hippocampal tissues from the euthanized mice (n = 3). For all error bars, ± s.e.m. Full scans of all the blots are in Supplementary Note.

METHODS

***C. elegans* strains and genetics.** Standard *C. elegans* strain maintenance[51,52] procedures were followed. Nematode rearing temperature was kept at 20°C, unless noted otherwise. The following strains were used in this study: N2: wild type Bristol isolate, RB809: *ptl-1(ok621)III*, CL2120: *dvIs14 [(pCL12)* p_{unc-54}Abeta 1-42 + *(pCL26)* p_{mtl-2}*GFP*], *pink-1(tm1779)II, dct-1(tm376)X,* VC1024: *pdr-1(gk448)III*, CL2241: *dvIs50* [p_{snb-1}Abeta 1-42; *rol-6(su1006)*] , CL2355: *dvIs50* [p_{snb-1}Abeta 1-42; p_{mtl-2}GFP] I, BR5271: *byIs162*[p_{rab-3}F3(delta)K280 I277P I380P + p_{myo-2}mCherry], BR5270: *byIs161*[p_{rab-3}*F3ΔK280; *p_{myo-2}*mCherry*], *dvIs50* [p_{snb-1}Abeta 1-42;p_{mtl-2}GFP]I; *pink-1(tm1779)II*, *dvIs50*[p_{snb-1}Abeta 1-42;p_{mtl-2}GFP]I; *dct-1(tm376)X*, *dvIs50* [p_{snb-1}Abeta 1-42;p_{mtl-2}GFP]I; *pdr-1(gk448)III*, *pink-1(tm1779)II; byIs161*[p_{rab-3}*F3ΔK280; *p_{myo-2}*mCherry*], *dct-1(tm376)X; byIs161*[p_{rab-3}*F3ΔK280; *p_{myo-2}*mCherry*], *pdr-1(gk448)III*; *byIs161*[p_{rab-3}*F3ΔK280; *p_{myo-2}*mCherry*]. To monitor neuronal mitophagy, we used IR1864: N2; *Ex001*[$p_{unc-119}$TOMM-20::Rosella] transgenic animals. To examine DCT-1 and LGG-1 interaction *in vivo* in neurons*,* we used the following transgenic animals, IR2160: N2; *Ex002*[p_{rab-3}DsRed::LGG-1;p_{rab-3}DCT-1::GFP; p_{myo-2}*GFP*], IR2162: N2; *byIs161*[p_{rab-3}*F3ΔK280; *p_{myo-2}*mCherry*]; *Ex002*[p_{rab-3}DsRed::LGG-1; p_{rab-3}DCT-1::GFP; p_{myo-2}*GFP*], IR2161: N2; *dvIs50*[p_{snb-1}Abeta1-42; *rol-6(su1006)*]; *Ex002*[p_{rab-3}DsRed::LGG-1; p_{rab-3}DCT-1::GFP; p_{myo-2}*GFP*]. To monitor neuronal autophagy, we used IR308: N2; *Ex001*[p_{mec-7}GFP::LGG-1; *rol-6(su1006)*] and IR2379: N2; *Ex010*[p_{rab-3}DsRed::LGG-1] transgenic animals. To monitor general autophagy, we used the following transgenic animals, VIG9: *unc119(ed3)III*; *Is*[*unc-119(+);*p_{lgg-2}GFP::LGG-2], DA2123: N2; *adIs2122* [p_{lgg-1}GFP::LGG-1; *rol-6(su1006)*] and MAH145: N2; *sqEx4* [p_{atg-18}ATG-18::GFP; *rol-6(su1006)*].

Molecular cloning. To generate the p_{rab-3}DCT-1::GFP reporter construct, we fused a *BglII* fragment, containing the coding sequence of DCT-1::GFP, amplified from p_{dct-1}DCT-1::GFP reporter construct using the primers 5' AGATCTATGTCCATCTTTCTTGAGTTTG 3' and 5' AGATCTCTATTTGTATAGTTCATCCATGC 3', downstream of *mec-7* promoter in the pPD96.41 plasmid vector. Then, we removed the *mec-7* promoter and inserted a *SphI/XmaI* fragment containing the *rab-3* promoter, amplified from *C. elegans* genomic DNA using the primers 5' GCATGCATTTGCTTCTATTCCGTCCT 3' and 5' ACCGGTCCCGGGCTGAAAATAGGGCTACTGTAGAT 3, upstream of DCT-1::GFP. To generate p_{rab-3}DsRed::LGG-1, we inserted an *AgeI/EcoRI* fragment (derived from p_{lgg-1}DsRed::LGG-1), containing the coding sequence of *DsRed* downstream of the *mec-7* promoter of the pPD96.41 plasmid vector. We then fused an *EcoRI* fragment (derived from p_{lgg-1}DsRed::LGG-1) containing the coding sequence of *lgg-1* at the C terminus of DsRed of the p_{mec-7}DsRed. Then, we removed the *mec-7* promoter and inserted a *SphI/AgeI* fragment containing the *rab-3* promoter. The translational p_{rab-3}DCT-1::GFP and p_{rab-3}DsRed::LGG-1 fusion constructs were co-injected with p_{myo-2}GFP transformation marker into the gonads of wild type animals. To generate $p_{unc-119}$TOMM-20::Rosella, we removed the *myo-3* promoter form p_{myo-3}TOMM-20::Rosella described previously[10] and we inserted an *HindIII/XbaI* fragment (derived from the $p_{unc-119}$CTS-1::mCherry[10]) containing *unc-119* promoter upstream of the coding sequence of TOMM-20::Rosella biosensor. The translational $p_{unc-119}$TOMM-20::Rosella fusion construct was co-injected with pRF4 (*rol-6(su1006)* dominant transformation marker) into the gonads of wild type animals.

Screening of neuronal mitophagy inducers. Neuronal mitophagy inducers were

screened using two mitophagy detection nematode lines, *Ex*[$p_{unc-119}$mtRosella] and *Ex*[p_{rab-3}DCT-1:GFP;p_{rab-3}DsRed::LGG-1]. Our small compound library consists in-house synthesized small compounds for AD treatments (by Dr. Nigel Greig, NIH) and commercially available known autophagy/mitophagy inducers. For the *in vivo* drug screening, nicotinamide mononucleotide (NMN) was used as a positive control while the solvent (1%DMSO) was as negative control. Neuronal mitophagy events were quantified using the z scores of the colocalization between LGG-1/DCT-1. A screening window coefficient, called Z-factor, was used for evaluation and validation, with z-score of 0.5 to 1.0 means that the drug screen is deemed acceptable[23]. An agent with values higher than wild type ($p<0.05$) was scored as a mitophagy inducer.

***C. elegans* memory assays.** Chemotaxis to volatile compounds was performed at 25^{o}C, on 9 cm agar plates as described previously[31,53]. The chemotaxis index was calculated by subtracting the number of animals found at the trap from the number of animals at the source of the chemical, divided by the total number of animals subjected to the assay[31]. The resulting values were expressed as percentiles. For conditioning to isoamyl alcohol, a droplet of 5 µl pure isoamyl alcohol was placed on the lid of a conditioning non-bacterial seeded NGM plate. Animals were conditioned to isoamyl alcohol for 90 min. Both naive and conditioned animals were exposed for 90 min to isoamyl alcohol (gradient sources: isoamyl alcohol: 1/100 dilution in water). 1-day-old adult hermaphrodites were used in behavioral assays. Three distinct populations of 300 – 400 adults (for each strain) were scored during the assay period. For all experiments, NMN (5 mM) and AC (1 mM) were treated for 2 generations, while UA (0.1 mM) was treated from eggs for 1 generation. Two to four technical repeats for all worm experiments.

Mitophagy/autophagy detection. Mitophagy was detected by several methods in multiple model organisms as we reported previously[10,12,24]. Postmortem hippocampal brain tissues of AD patients and sex- and age-matched healthy controls were from Harvard brain bank (7 for each), and mitophagy was evaluated using electron microscopy (EM, and by a US Certified Electron Microscopist), western blot, and the co-localization between TOMM20 (Santa Cruz antibody #SC17764 at 1:500 dilution, then 2nd antibody FITC D&M) and LAMP2 (Novus antibody # NBP2-22217 at 1:200 dilution, then 2nd antibody CY3 D&R) (n = 3/group). For mitophagy in mouse brain tissues, we used a commercial mitophagy detection kit (Dojindo, #MD01-10) to detect mitophagy in neurons isolated from mouse tissue[24], and further the fresh-fixed tissues were subjected to EM. EM was used to evaluate mitophagic events in neurons and microglia of hippocampal and PFC tissues from mice. 25-30 images were taken for neurons and microglia, independently, for each mouse sample, and data were analyzed in a double-blind manner. Mitophagy = (number of mitochondria undergoing mitophagy incidence/total number of mitochondria per ROI). Neuronal mitophagy in *C. elegans* was measured using two strains. Firstly, we generated transgenic animals expressing pan-neuronal mitochondria-targeted Rosella biosensor (mtRosella) that combines a GFP variant sensitive to the acidic environment of the lysosomal lumen, fused to the pH-insensitive DsRed. Mitophagy was calculated as GFP/DsRed, thus the lower ratio of pixel intensity, the higher mitophagy. We also generated transgenic nematodes expressing DCT-1 mitophagy receptor fused with GFP together with autophagosomal marker LGG-1 fused with DsRed in neurons: *Ex*[p_{rab-3}DCT-1:GFP; p_{rab-3}DsRed::LGG-1]. Mitophagy was assessed using the pearson's coefficient between LGG-1/DCT-1 co-localization. Stress-induced mitophagy was evaluated by

treating the *Ex*[p_{rab-3}DCT-1:GFP; p_{rab-3}DsRed::LGG-1] worms with paraquat/Para. (final concentration 8 mM). The CL2241, BR5270, and other designated strains were then crossed with these mitophagy strains to monitor mitophagy levels in transgenic Alzheimer's Disease models. For all nematode experiments, NMN (5 mM) and AC (1 mM) were treated for 2 generations, while UA (0.1 mM) was treated from eggs for 1 generation. Unless specified, adult Day 1 worms were used for experiment. Detailed information on *in vivo* mitophagy assessment in nematodes and data analysis were described elsewhere[10,24]. The autophagic flux, including autophagosomes and autolysosomes, was quantified using a monomeric red fluorescent protein (mRFP)-GFP tandem fluorescent-tagged LC3 plasmid (ptfLC3) [11,20].

iPSC-derived neurons. iPSCs were differentiated into cortical neurons using the protocols reported previously[17,18]. Briefly, iPSCs were maintained in an adherent monolayer on matrigel-coated plates, followed by neural induction using dual SMAD inhibition (10 μMSB431542, 1 μM dorsomorphin) in neural maintenance media (DMEM/F-12, neurobasal, B-27, N-2, 5 μg/ml insulin, 1mM L-glutamine, 100 μM NEAAs, 100 μM 2-mercaptoethanol, 1x penicillin and streptomycin). Cells were then passaged as small clusters onto coated wells (with poly-L-ornithine and laminin) after the formation of a neuro-epithelial sheet. Subsequent differentiating cells formed neural rosettes in the presence of b-FGF. Cells were subsequently passaged and underwent final single cell plating at day 30. We confirmed the cortical identity using RT-qPCR and immunofluorescence microscopy. Cortical cultures were maintained in neural maintenance media with 100 μg/ml of laminin feeding every ten days to inhibit cell detachment.

Evaluation of phosphorylated Tau (p-Tau) in cell lines. Three cell lines, including 2N4R, 1N4R, and 2N3R-overexpressed SH-SY5Y cells (generated by Dr. Mansour Akbari) were used for pTau evaluation. Cells were treated with UA (50 μM) for 24 h, followed by evaluation of p-Tau using aforementioned western blot.

Mice. All animal experiments were performed and approved by NIA Animal Care and Use Committee, and were in compliance with all relevant ethical regulations. All the animals were maintained at the National Institute on Aging under standard conditions and fed standard animal chow. The APP/PS1 mouse strain (#stock number 004462 in Jackson's laboratory) was from Prof. Mark Mattson's laboratory. APP/PS1 mice and their WT littermates were used for experiments. The APP/PS1 mice were treated with UA (200 mg/kg/day) or AC (30 mg/kg/day) by gavage starting from 6 months (the age at which Aβ plaques appear) to 8 months, and subsequently evaluated for behavioral and molecular endpoints. The 3xTgAD mouse strain was generated as described previously[56]. The 13-month-old 3xTgAD mice were treated with UA (200 mg/kg/day) by oral gavage for 1 month, and subsequently evaluated for behavioral and molecular endpoints.

Morris Water Maze and Y Maze. The Morris water maze (MWM) test was performed as previously described[57]. The device is a circular pool (140 cm diameter) filled with water that is maintained at 22˚C. The pool was painted with non-toxic white paint. A 12-cm diameter transparent platform was placed 1 cm below the water surface at a fixed position. Mice were trained for 7 consecutive days, with 4 trials per day. Each trial lasted 60 s or until the mouse found the platform. If the platform was not found during the time period, the experimenter directed the mouse to the platform. After each trial,

the mouse was placed on the platform for 30 s. On the 7th day, after completing the training phase, the platform was removed for the 60 s probe trial. All parameters were recorded by a video tracking system (Anymaze, Stoelting). The Y Maze Spontaneous Alternation Performance test (SAP) measures the ability to recognize a previously explored environment. The maze consisted of three arms (8 × 30 × 15 cm), with an angle of 120 degrees between each arm. The numbers of entries and alterations were recorded using the Anymaze tracking system. Mice were introduced into the center of the Y maze and allowed to freely explore the maze for 10 min. Between trials the arms were cleaned with 70% ethanol solution. SAP is the subsequent entry into a novel arm over the course of 3 entries and the % SAP is calculated by the number of actual alternations/ (total arm entries-2) × 100[58]. For the APP/PS1 mice-based behavioral studies, 11-13 mice/group were used. For 3xTgAD mice-based behavioral studies, 7 mice were used. No statistical methods were used to pre-determine sample sizes but our sample sizes are similar to those reported in previous publications (Hou Y, et al., PNAS 2018; Iaccarino HF et al., Nature 2016).

Object recognition test and Fear conditioning test. Object recognition test were performed as described previously[39]. The device was a Plexiglas box (25 × 25 × 25 cm). The mouse could explore two identical objects for 10 min during the training phase. 1 h later, the mouse was returned to the box, which had been modified to contain one familiar object and one novel object. To exclude olfactory cues, the boxes and objects were cleaned before each test. The automatic tracking system (ANY-Maze; Stoelting) was used to monitor exploration behavior. Exploration time was calculated as the length of time the mouse sniffed or pointed its nose or paws at the object. The “recognition index” refers to the time spent exploring the novel object relative to the time spent exploring both objects. Fear memory is measured by pairing a conditioned
stimulus (CS) to an unconditioned stimulus (US) as described. We used Video Freeze Conditioning software (Med Associates) to measure freezing behavior. On day one, mice were placed inside the chambers; after 120-s baseline, a 30-s CS tone followed, and a US foot shock was given during the last 2 s of the CS. This CS–US pairing was repeated two additional times during 180–220 s and 240–270 s. On day two, both contextual and cued phases were done. During phase one, mice were placed in the same testing chambers used on day one for 5 min. During phase two, 3 h later, mice were placed into modified chambers with plastic inserts, and after 300 s the CS tone was played for 30 s at 1-min intervals (five CS tones in total). After 10 min, mice were returned to their housing cages. For the APP/PS1 mice-based behavioral studies, 11-13 mice/group were used. For 3xTgAD mice-based behavioral studies, 7 mice were used. No statistical methods were used to pre-determine sample sizes but our sample sizes are similar to those reported in previous publications (Hou Y, et al., PNAS 2018; Iaccarino HF et al., Nature 2016).

Electron microscopy. Ultrastructure of mitochondrial morphology was visualized and imaged using electron microscopy (EM) by a US Certified Electron Microscopist Dr. J. Bernbaum. Images for neurons, astrocytes, and microglia were taken independently. Quantification of mitochondrial parameters in different cell types were performed using ImageJ (length, diameter, and area). Percentage of damaged mitochondria as well as mitophagic-like events were calculated. All quantifications were performed in a double-bind manner.

Microarray. Gene expression analysis was performed on hippocampal tissue from APP/PS1 and wild type littermates. RNA was purified with Nucleospin RNA isolation kit (Macherey-Nagel, #740955.250) with initial quantitation conducted using a NanoDrop ND-1000 spectrophotometer. The quality of the RNA was inspected using a 2100 Bioanalyzer (Agilent Technologies). The microarray was performed by the Gene expression and Genomics core facility (NIA) and analyzed using DIANE 6.0 software. The complete set was tested for Geneset enrichment using parametric analysis of gene set enrichment (PAGE). Detailed data analysis was performed as we reported previously[59].

Immunohistochemistry and immunofluorescence. Briefly, anesthetized mice were perfused with 1x PBS and then with 4% paraformaldehyde (PFA) in PBS. The collected brains were placed in 4% PFA for 24 h and then equilibrated in 30% sucrose for 24 h. 1:8 series equidistant floating 30-μm coronal sections (interval 240 μm) were prepared, including dentate gyrus (DG) area. Approximately 9-10 slices of each mouse were incubated in blocking buffer (10% donkey serum and 0.3% Triton X-100 in PBS) for 30 min at room temperature (RT). Thereafter, samples were incubated overnight with the primary antibody at 4°C and then incubated with the appropriate fluorescent probe conjugated secondary antibodies for 1 h at RT protected from light. Nuclei were stained with DAPI at 1:5000 dilution. The pictures were taken using an Axiovert 200M Zeiss microscope (Zeiss). Specific primary antibodies used include rabbit anti-GFAP (DAKO, #Z033401-2), mouse anti-6E10 for Aβ (BioLegend, #803002), and goat anti-IBA1 (NOVUS, #NB100-1028) antibodies. To evaluate Aβ plaques, tissues were stained with 6E10 antibody to recognize Aβ (1:500, BioLegend, #803002) and anti-GFAP antibody (1:500 DAKO, #Z033401-2) to recognize astrocytes. Plaque numbers per region of interest (ROI) were counted and quantified. Microglia were stained with anti-IBA1 antibody (NOVUS, #NB100-1028), and morphological changes were assessed by measuring processes/microglial cell and average process length (μm)[30]. To evaluate phagocytosis, we used = (numbers of microglia with Aβ plaques per RIO)/(total numbers of microglia per RIO). For immunofluorescence, iPSC-derived neurons were stained with designated antibodies, including MAP2 (abcam, #AB5392, 1:10000), BRN2 (Santa Cruz, #sc-6029, 1:300), TBR1 (abcam, #ab31940, 1:1000), TUJ1 (abcam, #ab18207, 1:1000), followed by 2nd antibody staining, and imaging in a Leica confocal microscope.

Western Blots. Human postmortem brain tissues from AD patients and healthy controls were obtained from Harvard Brain bank. Western blot analyses were performed as described previously[11,12]. Briefly, samples (e.g., human iPSC-derived neurons, postmortem human hippocampal brain samples, and mouse brain samples) were collected and prepared using 1x RIPA buffer (Cell Signaling, #9806S) containing protease inhibitors (Bimake, #B14002) and phosphatase inhibitors (Bimake, #B15002). Proteins were separated on 4-12% Bis-Tris gel (ThermoFisher Scientific, #NP0336BOX) or 4-15% Criterion TGX precast midi protein gel (Bio-Rad, #5671085) and probed with antibodies. Chemiluminescence detection was performed using a ChemiDoc XRS System. Gamma adjustment was used to reduce dark background when necessary. Quantification was performed using ImageJ. Antibodies used were: PAR (TREVIGEN, #4336-BPC-100), PARP1 (Cell signaling, #9542), β-actin (Santa Cruz, #sc-1616), Bcl-2 (Santa Cruz, #sc-7382), SOD2 (Enzo, #AD1-SOD-110-F), AMPK (Cell signaling, #5831), pAMPK (Thr172) (Cell signaling, #2535), pMFF (Ser146) (Cell signaling, #49281), MFF (Cell signaling, #86668), PINK1 (Novus,

#BC100-494), Parkin (Cell signaling, #2132), pTBK1 (Ser172) (Cell signaling, #5483), TBK1 (Cell signaling, #3504), pULK1 (Ser555) (Cell signaling, #5869), ULK1 (Cell signaling, #6439), p62 (Cell signaling, #39749), tau (Cell signaling, #46687), pTau (Thr181) (Cell signaling, #12885), pTau (Thr231) (abcam, #ab151559), pTau (Ser262) (abcam, #ab4856), pTau (Ser202/Thr205) (Thermofisher,#MN1020) γH2AX (Cell signaling, #9718), Caspase-3 (Cell signaling, #9662), total OXPHOS human WB antibody cocktail (abcam, #ab110411), pDRP1 (Cell signaling, #4494), DRP1 (Cell signaling, #8570), Mitofusin2 (Cell signaling, #11925), SOD1 (Cell signaling, #2770), SOD2 (Cell signaling, #13141), OPTN (Cell signaling, #58981), Bcl2L13 (ThermoFisher, # PA5-15043), FUNDC1 (ThermoFisher, # PA5-49413), NIX/BNIP3L (Cell signaling, #12396), Beclin1 (Cell signaling, #3495), LC3 (Novus, #NB100-2220), PSD95 (Cell signaling, #3450), SIRT1 (Cell signaling, #8469), PGC1α (Cell signaling, #2178), REST (abcam, #ab21635), AMBRA1 (Cell signaling, #24907), IL-10 (Novus, #AF519), NLRP3 (Adipogen, #AG-20B-0014-C100), Caspase-1 (Proteintech, #22915-1-AP), CD68 (Abcam, #ab955), IRF7 (Abcam, #ab109255), CSF2RA (Thermofisher, #PA5-37358), osteopontin (Abcam, #ab8448) Synaptophysin (Cell signaling, #5461), Tuj-1 (Cell signaling, #5568) and MUL1 (abcam, #ab84067). All other first antibodies were obtained from Cell signaling. Second antibodies including anti-mouse IgG (#NA931V) and anti-rabbit IgG (NA934V) were from GE Healthcare, and anti-goat IgG were from Sigma-Aldrich (#A8919). For dilution fold, 1st antibodies were used at 1:1000 (unless otherwise stated elsewhere), with 2nd antibodies used at 1:10000 (unless otherwise stated elsewhere). All the antibodies were validated for use in mouse/human tissues based on previous publications (Fang EF et a., Cell 2014 [11]; Fang EF et al., Cell Metabolism 2016 [12]; Iaccarino HF et al., Nature 2016 [30]; Lazarou M et al., Nature 2015 [16]). Furthermore, detailed antibody validation profiles are available in the website of designated companies.

ELISA for Aβ and pro/anti-inflammatory cytokines. Mouse hippocampal and PFC extracts were prepared as previously reported[60]. The accumulation of human $A\beta_{1-40}$ and $A\beta_{1-42}$ was quantified by ELISA (ThermoFisher Scientific, #KHB3442, #KHB3482). Microglia were isolated from WT and APP/PS1 mice cortex and hippocampus using fluorescence activated cell sorting method and $CD11b^{+}CD45^{low}$ cells were isolated. The used antibodies were Pacific Blue CD11b (Biolegend, #101224) and Alexa Fluor 647 CD45 (Biolegend, #103124). Cultured microglia were treated with Pink1 siRNA (Dharmacon, E-004030-00-0005) for 72 hr and then treated with 50 μM UA for 24 hr. The supernatants were analyzed by ELISA. Kits for cytokines were from R&D systems, including TNFα (#MTA00B), IL-6 (#M6000B), IL-10 (#M1000B).

Oxygen consumption rate. We performed oxygen consumption rate (OCR) using SeaHorse Bioscience methodology for both iPSC-derived neurons and *C. elegans*. The iPSC-derived cortical neurons were differentiated according to the protocol aforementioned in an Agilent SeaHorse cell culture 96-well microplate. The neurons were treated with urolithin A (UA; 50 μM) for 24 hours. The sensor cartridge was hydrated with SeaHorse Bioscience XF96 calibrant overnight in the Prep Station (37°C, w/o CO_2) before running the cell culture microplate. Test assay medium was prepared by adding 2 mM L-glutamine (Life Technologies, 25030-081), 10 mM glucose (Sigma, G7528), 5 mM pyruvate (Sigma, S8636) into XF Base Medium (Agilent Technologies, Cat. 102353-100) prior to wash the microplate using the pre-prepared assay medium according to the instructions by SeaHorse Bioscience. Then culture microplate was

placed in a 37°C incubator without CO_2 for an hour prior to the assay. The sensor cartridge was prepared by adding 25 µL of assay medium to port A with 2 µM oligomycin (Sigma, 495455), to port B with 2 µM FCCP (Sigma, C2920), to port C mixed with 1 µM rotenone (Sigma, R8875), and 1 µM antimycin A (Sigma, A8674). After the run was completed, the cell microplate medium was replaced with PBS, transferred to a -80°C freezer overnight. The protein concentration was determined using a BCA protein assay (ThermoFisher Scientific), and used to normalize the SeaHorse XF96 primary data. OCR of *C. elegans* was measured per previous methods using a Seahorse XFe96 instrument (Seahorse Bioscience Inc.) [61,62]. Briefly, 200 L4 nematodes/group were transferred to designated drug plates, followed by OCR detection on adult day 3. On the day of the experiment, all the worms were collected, followed by washing with M9 buffer three times. Worms were then re-suspended and transferred in 96-well standard Seahorse plates (#100777–004) (10~15 worms per well), and OCRs at different conditions (FCCP, sodium azide) was measured six times. After the experiments, worm numbers were counted, followed by data normalization to the number of worms in each individual well. Six replicates were performed for each group, and the experiment was repeated two-three times.

Mitochondrial parameters. Parameters including mitochondrial ROS production and ATP level were assessed to evaluate mitochondrial function. For mitochondrial ROS, isolated neurons were stained with MitoSOX (3 µM for 30 min), followed by fluorescence determination using a flow cytometer (BD ACCURI C6 PLUS)[11]. Flow data were analyzed using FCS Express 4 software. ATP levels in the postmortem human brain samples and the iPSC-derived neurons were detected using a standard commercial kit (abcam#ab113849). For the detection of mitochondrial ROS in worms, worms were treated with UA (0.1 mM) from L4 to adult day 3, followed by isolation of fresh mitochondria which were then stained with a ROS dye DCFDA (abcam #ab113851, 25 µM for 45 min) [63,64], followed by running FACS for signal quantification. We followed a standard protocol for gating strategy[65], please see the figure in the link exemplifying the gating strategy (https://www.nature.com/articles/nprot.2017.133/figures/7).

Randomization and blinding. Animal/samples (mice) were assigned randomly to the various experimental groups, and mice were randomly selected for behavioral experiments. In data collection and analysis (e.g., mouse behavioral studies, mouse imaging data analysis, as well as imaging and data analysis of EM), the performer(s) was blinded with experimental design.

Statistical analysis. GraphPad Prism 6.0 was used for statistical analysis. Data shown is mean ± SEM with $p < 0.05$ considered statistically significant. Two-tailed unpaired t-test was applied for comparisons between two groups. Group differences were analyzed with one-way ANOVA followed by Sidak's multiple comparisons test or two-way ANOVA followed by Tukey multiple comparisons test for multiple groups. Data distribution was assumed to be normal but this was not formally tested. No statistical methods were used to predetermine sample sizes, but our samples sizes (mouse experiments) are similar to those reported in previous publications (Hou Y, et al., PNAS 2018 [39]; Iaccarino HF et al., Nature 2016 [30]).

Life Sciences Reporting Summary. Further information on research design is available in the “Life Sciences Reporting Summary” linked to this article.

Software used and Code availability. ANY-maze (version 4.99) was used for behavioral tracking in the mouse studies. ZEN (blue edition) software was used for taking images. FCS Express 4 was used for flow cytometry. Microsoft Excel (2016) and Graphpad Prism 7 software were used for data analysis. ImageJ with the plug in ObjectJ (https://sils.fnwi.uva.nl/bcb/objectj/download/) was used for morphological quantification of mitochondria.

Data availability. The microarray GEO accession number for the data reported in this paper is GSE111737. All data are available from the corresponding author upon reasonable request.

Additional information

Supplementary information is available for this paper at

Reprints and permissions information is available at www.nature.com/reprints.

Correspondence should be addressed E.F.F. (e.f.fang@medisin.uio.no) or V.A.B. (bohrv@grc.nia.nih.gov). Requests for materials should be addressed to E.F.F., V.A.B., or N.T. (tavernarakis@imbb.forth.gr).

Additional References

51. Brenner, S. The genetics of Caenorhabditis elegans. Genetics 77, 71-94 (1974).
52. Samara, C., Syntichaki, P. & Tavernarakis, N. Autophagy is required for necrotic cell death in Caenorhabditis elegans. Cell Death Differ 15, 105-112 (2008).
53. Bargmann, C.I. & Horvitz, H.R. Chemosensory neurons with overlapping functions direct chemotaxis to multiple chemicals in C. elegans. Neuron 7, 729-742 (1991).
54. Brewer, G.J. & Torricelli, J.R. Isolation and culture of adult neurons and neurospheres. Nat Protoc 2, 1490-1498 (2007).
55. Palikaras, K. & Tavernarakis, N. Assessing Mitochondrial Selective Autophagy in the Nematode Caenorhabditis elegans. Methods Mol Biol 1567, 349-361 (2017).
56. Oddo, S. et al. Triple-transgenic model of Alzheimer's disease with plaques and tangles: intracellular Abeta and synaptic dysfunction. Neuron 39, 409-421 (2003).
57. Vorhees, C.V. & Williams, M.T. Morris water maze: procedures for assessing spatial and related forms of learning and memory. Nat Protoc 1, 848-858 (2006).
58. Ghosal, K. et al. Alzheimer's disease-like pathological features in transgenic mice expressing the APP intracellular domain. Proc Natl Acad Sci U S A 106, 18367-18372 (2009).
59. Scheibye-Knudsen, M. et al. A high-fat diet and NAD(+) activate Sirt1 to rescue premature aging in cockayne syndrome. Cell Metab 20, 840-855 (2014).
60. Hou, Y. et al. Smart Soup, a traditional Chinese medicine formula, ameliorates amyloid pathology and related cognitive deficits. PLoS One 9, e111215 (2014).
61. Koopman, M. et al. A screening-based platform for the assessment of cellular respiration in Caenorhabditis elegans. Nat Protoc 11, 1798-1816 (2016).
62. Fang, E.F. et al. Tomatidine enhances lifespan and healthspan in C-elegans through mitophagy induction via the SKN-1/Nrf2 pathway. Sci Rep-Uk 7 (2017).
63. Forester, C.M. et al. Revealing nascent proteomics in signaling pathways and cell differentiation. Proc Natl Acad Sci U S A 115, 2353-2358 (2018).
64. Skamagki, M. et al. ZSCAN10 expression corrects the genomic instability of iPSCs from aged donors. Nat Cell Biol 19, 1037-1048 (2017).
65. Yuan, H. et al. Heat-induced radiolabeling and fluorescence labeling of

Feraheme nanoparticles for PET/SPECT imaging and flow cytometry. Nat Protoc 13, 392-412 (2018).

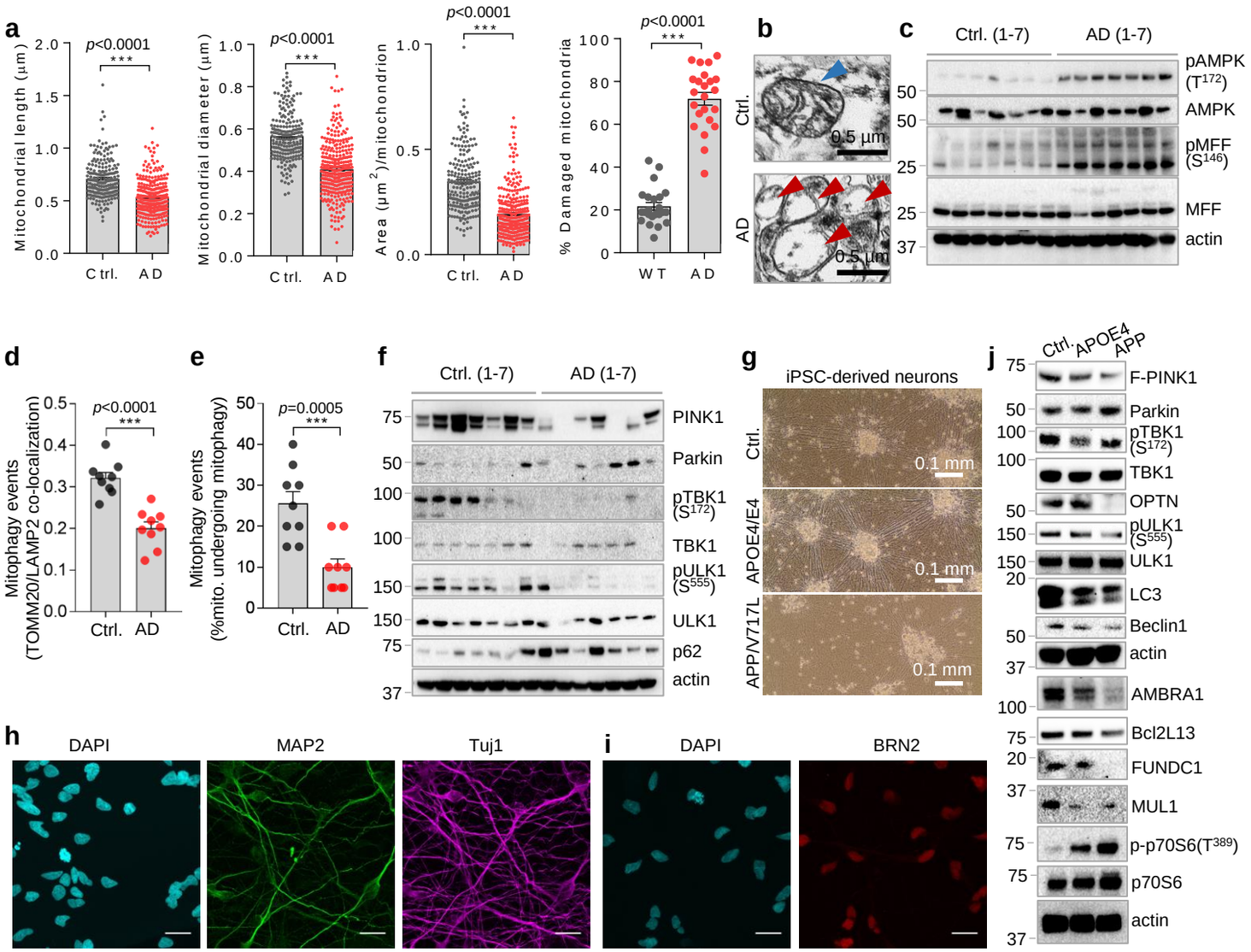
a
Mitochondrial length (μm)
p<0.0001
***
C trl.
A D
Mitochondrial diameter (μm)
p<0.0001
***
C trl.
A D
Area (μm²)/mitochondrion
p<0.0001
***
C trl.
A D
% Damaged mitochondria
p<0.0001
***
W T
A D
b
Ctrl.
AD
0.5 μm
0.5 μm
c
Ctrl. (1-7)
AD (1-7)
pAMPK (T172)
AMPK
pMFF (S146)
MFF
actin
d
Mitophagy events (TOMM20/LAMP2 co-localization)
p<0.0001
***
Ctrl.
AD
e
Mitophagy events (%mito. undergoing mitophagy)
p=0.0005
***
Ctrl.
AD
f
Ctrl. (1-7)
AD (1-7)
PINK1
Parkin
pTBK1 (S172)
TBK1
pULK1 (S555)
ULK1
p62
actin
g
iPSC-derived neurons
Ctrl.
APOE4/E4
APP/V717L
0.1 mm
0.1 mm
0.1 mm
j
Ctrl.
APOE4
APP
F-PINK1
Parkin
pTBK1 (S172)
TBK1
OPTN
pULK1 (S555)
ULK1
LC3
Beclin1
actin
AMBRA1
Bcl2L13
FUNDC1
MUL1
p-p70S6(T389)
p70S6
actin
h
DAPI
MAP2
Tuj1
i
DAPI
BRN2

Figure 1

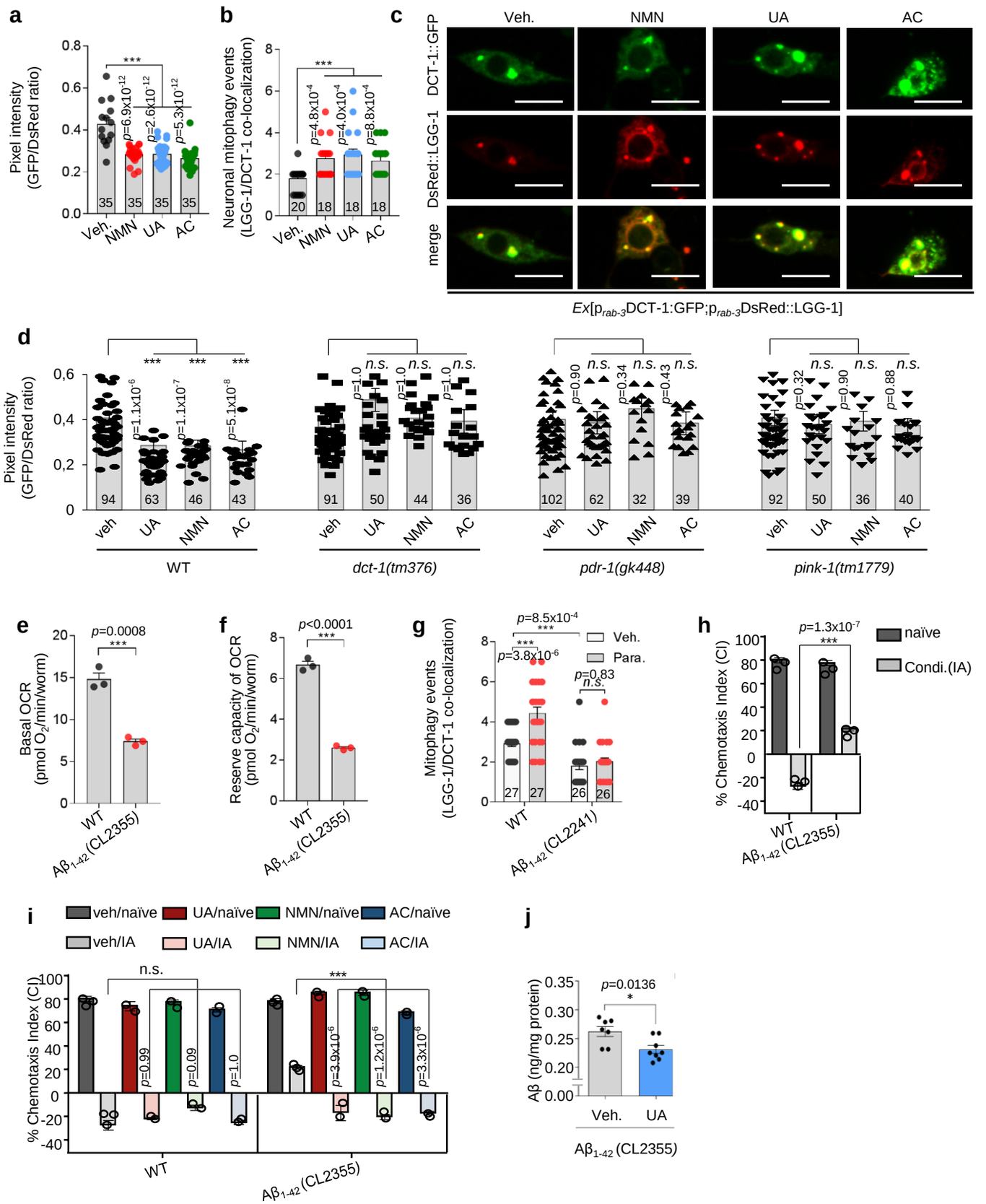
a
b
c
Pixel intensity (GFP/DsRed ratio)
Neuronal mitophagy events (LGG-1/DCT-1 co-localization)
Veh.
NMN
UA
AC
DCT-1::GFP
DsRed::LGG-1
merge
Ex[prab-3DCT-1:GFP;prab-3DsRed::LGG-1]
d
WT
dct-1(tm376)
pdr-1(gk448)
pink-1(tm1779)
e
Basal OCR (pmol O2/min/worm)
f
Reserve capacity of OCR (pmol O2/min/worm)
g
Mitophagy events (LGG-1/DCT-1 co-localization)
Veh.
Para.
h
% Chemotaxis Index (CI)
naïve
Condi.(IA)
i
veh/naïve
UA/naïve
NMN/naïve
AC/naïve
veh/IA
UA/IA
NMN/IA
AC/IA
% Chemotaxis Index (CI)
j
Aβ (ng/mg protein)
Aβ1-42 (CL2355)

Figure 2

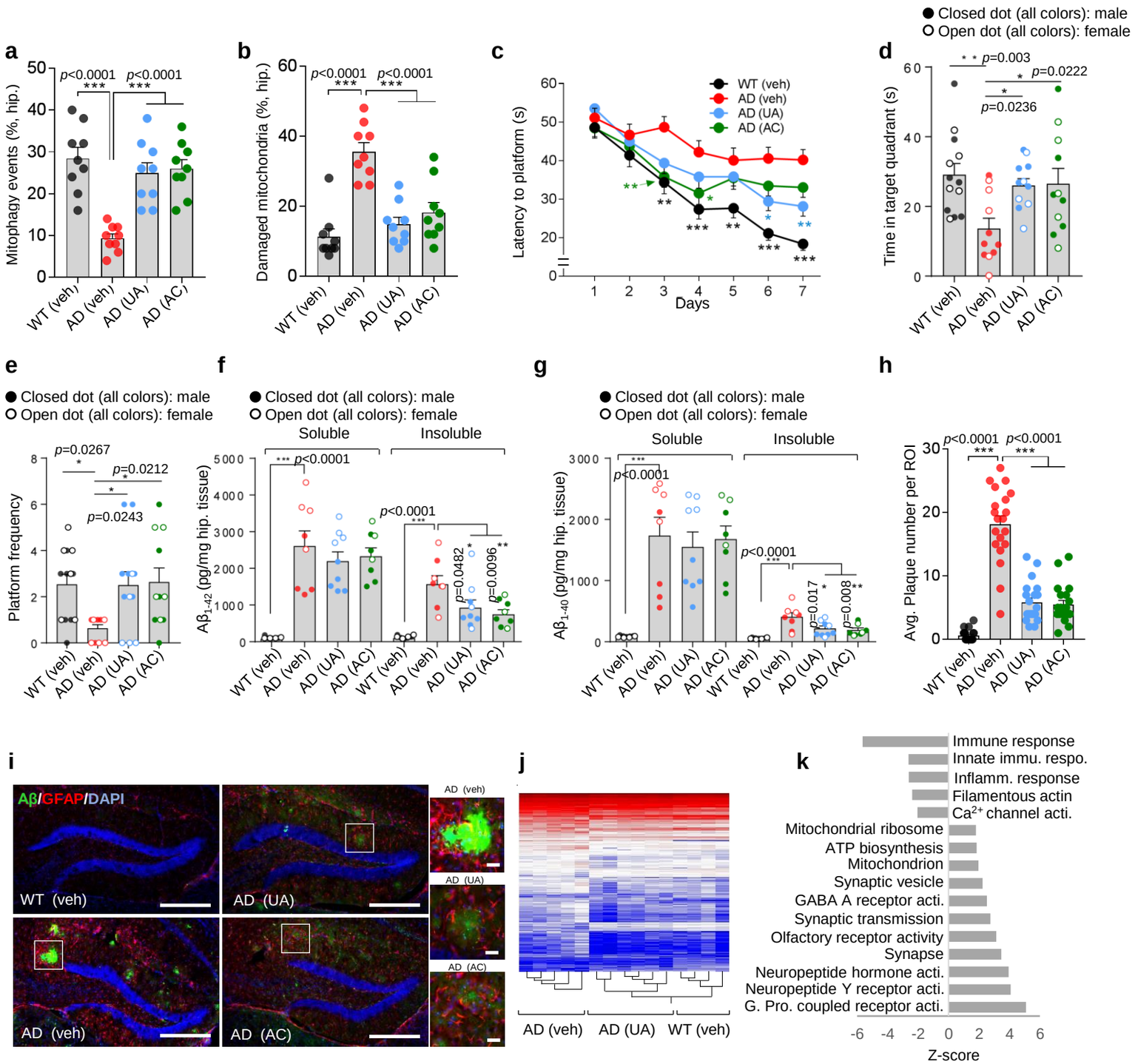
a
Mitophagy events (%, hip.)
p<0.0001
p<0.0001
WT (veh)
AD (veh)
AD (UA)
AD (AC)
b
Damaged mitochondria (%, hip.)
c
Latency to platform (s)
WT (veh)
AD (veh)
AD (UA)
AD (AC)
Days
d
Closed dot (all colors): male
Open dot (all colors): female
Time in target quadrant (s)
p=0.003
p=0.0222
p=0.0236
e
Platform frequency
p=0.0267
p=0.0212
p=0.0243
f
Soluble
Insoluble
Aβ1-42 (pg/mg hip. tissue)
p<0.0001
p=0.0482
p=0.0096
g
Aβ1-40 (pg/mg hip. tissue)
p<0.0001
p=0.017
p=0.008
h
Avg. Plaque number per ROI
i
Aβ/GFAP/DAPI
WT (veh)
AD (UA)
AD (veh)
AD (AC)
j
AD (veh)
AD (UA)
WT (veh)
k
Immune response
Innate immu. respo.
Inflamm. response
Filamentous actin
Ca2+ channel acti.
Mitochondrial ribosome
ATP biosynthesis
Mitochondrion
Synaptic vesicle
GABA A receptor acti.
Synaptic transmission
Olfactory receptor activity
Synapse
Neuropeptide hormone acti.
Neuropeptide Y receptor acti.
G. Pro. coupled receptor acti.
Z-score

Figure 3

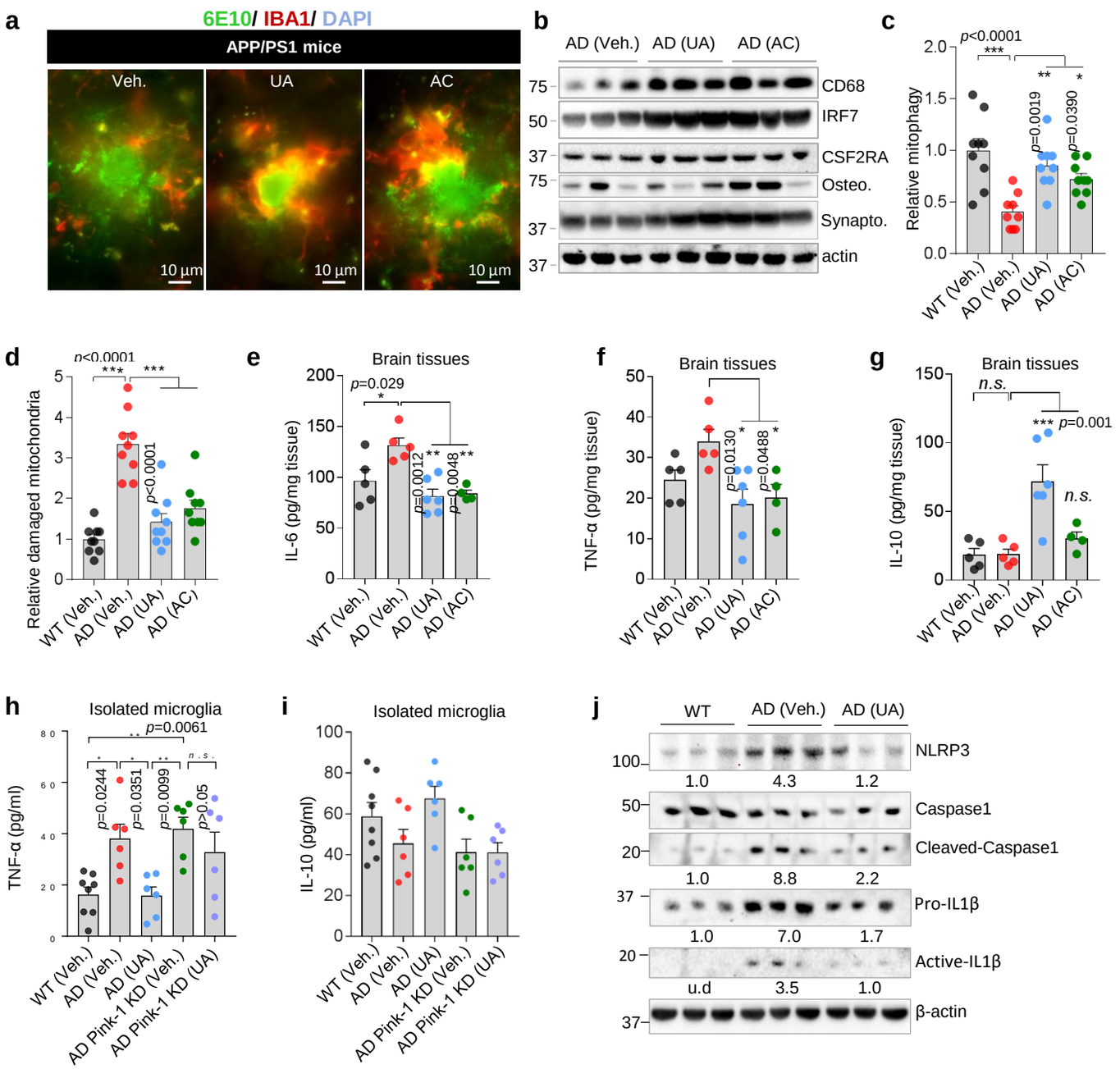
a
6E10/ IBA1/ DAPI
APP/PS1 mice
Veh.
UA
AC
10 µm
b
AD (Veh.)
AD (UA)
AD (AC)
CD68
IRF7
CSF2RA
Osteo.
Synapto.
actin
c
p<0.0001
p=0.0019
p=0.0390
Relative mitophagy
WT (Veh.)
AD (Veh.)
AD (UA)
AD (AC)
d
p<0.0001
p<0.0001
Relative damaged mitochondria
e
Brain tissues
p=0.029
p=0.0012
p=0.0048
IL-6 (pg/mg tissue)
f
Brain tissues
p=0.0130
p=0.0488
TNF-α (pg/mg tissue)
g
Brain tissues
n.s.
p=0.001
n.s.
IL-10 (pg/mg tissue)
h
Isolated microglia
p=0.0061
p=0.0244
p=0.0351
p=0.0099
p>0.05
TNF-α (pg/ml)
AD Pink-1 KD (Veh.)
AD Pink-1 KD (UA)
i
Isolated microglia
IL-10 (pg/ml)
j
WT
AD (Veh.)
AD (UA)
NLRP3
1.0
4.3
1.2
Caspase1
Cleaved-Caspase1
1.0
8.8
2.2
Pro-IL1β
1.0
7.0
1.7
Active-IL1β
u.d
3.5
1.0
β-actin

Figure 4

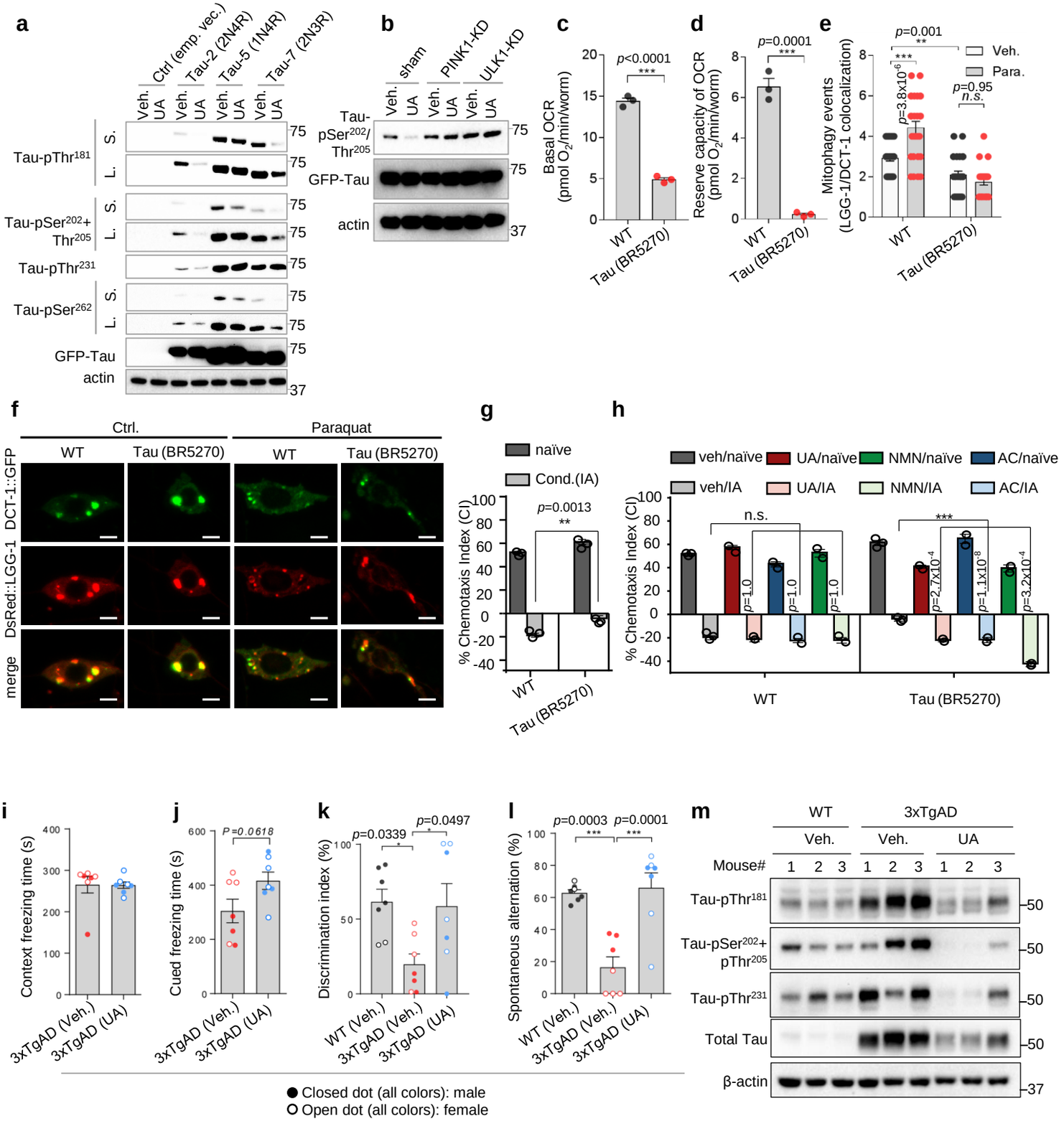
a
Ctrl (emp. vec.)
Tau-2 (2N4R)
Tau-5 (1N4R)
Tau-7 (2N3R)
Veh.
UA
Tau-pThr181
Tau-pSer202+ Thr205
Tau-pThr231
Tau-pSer262
S.
L.
GFP-Tau
actin
75
37
b
sham
PINK1-KD
ULK1-KD
Tau-pSer202/ Thr205
GFP-Tau
actin
c
Basal OCR (pmol O2/min/worm)
p<0.0001
WT
Tau (BR5270)
d
Reserve capacity of OCR (pmol O2/min/worm)
p=0.0001
e
Mitophagy events (LGG-1/DCT-1 colocalization)
p=0.001
p=3.8x10-6
p=0.95
n.s.
Veh.
Para.
f
Ctrl.
Paraquat
WT
Tau (BR5270)
DCT-1::GFP
DsRed::LGG-1
merge
g
naïve
Cond.(IA)
% Chemotaxis Index (CI)
p=0.0013
h
veh/naïve
UA/naïve
NMN/naïve
AC/naïve
veh/IA
UA/IA
NMN/IA
AC/IA
n.s.
p=1.0
p=2.7x10-4
p=1.1x10-8
p=3.2x10-4
i
Context freezing time (s)
3xTgAD (Veh.)
3xTgAD (UA)
j
Cued freezing time (s)
P=0.0618
k
Discrimination index (%)
p=0.0339
p=0.0497
WT (Veh.)
l
Spontaneous alternation (%)
p=0.0003
p=0.0001
m
WT
3xTgAD
Veh.
UA
Mouse#
Tau-pThr181
Tau-pSer202+ pThr205
Tau-pThr231
Total Tau
β-actin
50
37
Closed dot (all colors): male
Open dot (all colors): female

Figure 5